

Supporting information

Aerosol crosslinked crown ether diols melded with poly(vinyl alcohol) as specialized microfibrous Li⁺ adsorbents

*Lawrence A. Limjuco,^{†a} Grace M. Nisola,^{†a} Rey Eliseo C. Torrejos,^{†a} Jeong Woo Han,^b Ho Seong Song,^b Khino J. Parohinog,^a Sangho Koo,^c Seong-Poong Lee,^{*a} Wook-Jin Chung^{*a}*

^aEnergy and Environment Fusion Technology Center (E²FTC), Department of Energy Science and Technology (DEST), Myongji University, Myongji-ro 116, Cheoin-gu, Yongin City, Gyeonggi Province, Republic of Korea (17058)

^bDepartment of Chemical Engineering, University of Seoul, South Korea (02504)

^cDepartment of Chemistry, Myongji University, Myongji-ro 116, Cheoin-gu, Yongin City, Gyeonggi Province, Republic of Korea (17058)

[†]co-first authors

Corresponding authors:

**(W.-J. Chung) wjc0828@gmail.com; *(S.-P. Lee) spleemju2012@gmail.com.*

Tel.: (82)-31-330-6687; Fax: (82)-31-337-2902

Supporting Information (SI) Contents

<i>Number</i>	<i>Title</i>	<i>Page</i>
	Materials and reagents used in the study	S–6
	CE diol synthesis protocol	
Figure S1	Synthesis scheme of CE diols. (a) 2-step preparation of CE 1 via intermediate A ; (b) intermolecular cyclization of various bis-epoxides with catechol for CE 2 and CE 3.	S–7
	¹H and ¹³C NMR spectra of CE diols	
Figure S2	¹ H and ¹³ C NMR spectra of CE 1 intermediate: 1,1-phenyldioxy-bis(2,3-epoxypropane) denoted as CE 1 intermediate A .	S–8
Figure S3	¹ H and ¹³ C NMR spectra of CE 1: 6,7,8,15,16,17-hexahydrodibenzo[1,4,8,11] tetraoxacyclotetradecine-7,16-diol denoted as 2HDB14C4 .	S–9
Figure S4	¹ H and ¹³ C NMR spectra of CE 2: 7,7-dimethyl-3,4,6,7,8,10,11,12-octahydro-2H- benzo[1,4,8,12]tetraoxacyclopentadecine-3,11-diol denoted as 2HB2M15C4 .	S–10
Figure S5	¹ H and ¹³ C NMR spectra of CE 3: 2,3,4,6,7,8,9,11,12,13-decahydrobenzo[1,4,8,13] tetraoxacyclohexadecine-3,12-diol denoted as 2HB16C4 .	S–11
	Electrospinning conditions	
Table S1	Electrospinning conditions for the fabrication of MF adsorbents.	S–12
	Synthesis of methylated CEs (mCEs) for control MF samples	
Figure S6	Synthesis scheme of methylated CEs via etherification.	S–13
	Characterization results of mCE compounds	
Figure S7	FTIR spectra of methylated CEs (mCE 1 – 3).	S–14
Figure S8	¹ H and ¹³ C NMR spectra of mCE 1 : 7,16-dimethoxy-6,7,8,15,16,17-hexahydrodibenzo[b,i][1,4,8,11]tetraoxacyclotetradecine.	S–15
Figure S9	¹ H and ¹³ C NMR spectra of mCE 2 : 3,11-dimethoxy-7,7-dimethyl-3,4,6,7,8,10,11,12-octahydro-2H-benzo[b][1,4,8,12]tetraoxacyclopentadecine.	S–16

Figure S10	^1H and ^{13}C NMR spectra of mCE 3 : 3,12-dimethoxy-2,3,4,6,7,8,9,11,12,13-ecahydrobenzo[b][1,4,8,13]tetraoxacyclohexadecine.	S–17
	Calculations for MF stability tests	S–18
Table S2	List of equations used for the stability tests.	S–19
	Actual composition of MFs used for adsorption studies	S–18
	Calibration curves for PVA and CE concentrations in elution tests	
Figure S11	Calibration Curve for PVA [as C] via TOC analysis.	S–20
Figure S12	UV-Vis spectra of mCEs and CE diols with no interference from PVA.	S–20
Figure S13	Constructed standard curves for CE diols using UV-Vis spectrophotometry (5 – 100 mg L ⁻¹).	S–21
Figure S14	Constructed standard curves for methylated CEs (mCEs) using UV-Vis spectrophotometry (5 – 100 mg L ⁻¹).	S–21
	Sample UV-Vis spectra of elution samples	
Figure S15	Sample UV-Vis spectra of eluent samples from CE/PVA and mCE/PVA MFs. A spectrum for GA aqueous solution is overlaid.	S–22
Table S3	Integrated FTIR peaks and corresponding ratios.	S–23
	Elution test results and actual compositions of MFs used for adsorption experiments	
Table S4	Swelling ratio and measurements for the stability test of pure PVA, CE/PVA and mCE/PVA MFs.	S–24
Table S5	Component losses (CE and PVA) during elution tests and the final composition of MF samples used for adsorption experiments.	S–24
	^{13}C CP/MAS NMR results and peak interpretation	S–25
Figure S16	^{13}C CP/MAS NMR of pure PVA MF.	S–26
Table S6	Chemical shifts from ^{13}C CP/MAS NMR and peak assignments for pure PVA MF.	S–26
Figure S17	^{13}C CP/MAS NMR of CE 1/PVA MF.	S–27

Table S7	Chemical shifts from ^{13}C CP/MAS NMR and peak assignments for CE 1/PVA MF.	S–27
Figure S18	^{13}C CP/MAS NMR of CE 2/PVA MF.	S–28
Table S8	Chemical shifts from ^{13}C CP/MAS NMR and peak assignments for CE 2/PVA MF	S–28
Figure S19	^{13}C CP/MAS NMR of CE 3/PVA MF.	S–29
Table S9	Chemical shifts from ^{13}C CP/MAS NMR and peak assignments for CE 3/PVA MF	S–29

Broad bands at 70 ppm region

Figure S20	Chemical shift predications of $\text{CH}_2\text{-CH}_2$ in CE rings and $\alpha\text{-Cs}$ in crosslinked PVA and CEs using MestRenova 11.0.2.	S–30
-------------------	---	------

Morphology of uncrosslinked electrospun MFs

Figure S21	FE-SEM images of MFs before aerosol crosslinking (a) pure PVA and CE/PVA containing: (b) CE 1, (c) CE 2, and (d) CE 3.	S–32
-------------------	--	------

Surface analysis and mechanical test results of MF samples

Figure S22	Surface and mechanical properties of MF samples. (a) N_2 adsorption-desorption isotherms (Inset: pore size distribution); (b) Tensile strength, % elongation and Young's modulus.	S–33
-------------------	--	------

Adsorption properties

Figure S23	Adsorption results at varied solution pH ($C_0 = 7.35 \text{ mg L}^{-1}$; $m \cong 30 \text{ mg}$; $V = 50 \text{ mL}$; $T = 30^\circ\text{C}$).	S–35
Figure S24	Kinetic rate models for Li^+ adsorption in CE/PVA and pure PVA MFs: (a) pseudo-first and (b) pseudo-second order. ($C_0 = 7.35 \text{ mg L}^{-1}$; $m \cong 30 \text{ mg}$; $V = 50 \text{ mL}$; $T = 30^\circ\text{C}$; $\text{pH} = 8.1$).	S–36
Table S10	Li^+ adsorption performance of inorganic LIS reported in literature.	S–37
Table S11	Theoretical adsorption capacities of pure CEs.	S–38
Figure S25	Isotherm models for Li^+ adsorption in CE/PVA and pure PVA MFs: (a) Freundlich and (b) Langmuir. ($C_0 = 3 - 70 \text{ mg L}^{-1}$; $m \cong 30 \text{ mg}$; $V = 50 \text{ mL}$; $T = 30^\circ\text{C}$; $\text{pH} = 8.0$).	S–39
Table S12	Li^+ adsorption performance of CE-based Li^+ adsorbents reported in literature.	S–40

Density Functional Theory calculations

Table S13	Average opposite O distances, $[O-O]_{ave}$ before and after complexation of CEs with M^{n+} .	S-41
Table S14	O- M^{n+} distances (\AA) of CE- M^{n+} complexes calculated using DFT PBE-PAW level of theory.	S-42
Figure S26	Lowest energy conformation of free and 1:1 CE- M^{n+} complexed optimized using DFT PBE-PAW level of theory.	S-43

Exothermicity of exchange of reactions

Table S15	Binding enthalpies (ΔH) for the M^{n+} (CE) complexes.	S-44
Table S16	Binding enthalpies (ΔH) for the $M^{n+}(H_2O)_n$ where $n=6$.	S-44
Table S17	ΔH_n values of M^{n+} relative to Li^+ ($\Delta H_n = 0 \text{ kcal mol}^{-1}$).	S-45

Recycling experiments

Figure S27	Cycled Li^+ adsorption/desorption runs for regenerability tests of the CE/PVA MFs: (a) CE 1/PVA (b) CE 2/PVA and (c) CE 3/PVA. ($C_0 = 6.7 \text{ mg L}^{-1}$; $m \cong 30 \text{ mg}$; $V = 50 \text{ mL}$; $T = 30^\circ\text{C}$; $pH = 8.0$).	S-46
-------------------	---	------

MF autopsy after five adsorption/desorption cycles

Figure S28	SEM images of used CE/PVA MFs after 5 th adsorption/desorption cycle: (a) CE 1/PVA (b) CE 2/PVA and (c) CE 3/PVA.	S-47
Figure S29	UV-Vis spectra of stripping solutions (0.5 M HCl) used to desorb Li^+ from spent CE/PVA MFs (for eluted CE detection): (a) CE 1/PVA (b) CE 2/PVA and (c) CE 3/PVA.	S-48

List of Nomenclature	S-49
-----------------------------	------

References for Supporting Information	S-52
--	------

Materials and reagents used in the study

Bis-epoxide intermediates neopentyldiglycidyl ether (technical grade) and 1,4-bis(2,3-epoxypropyloxy)butane ($\geq 95\%$) were procured from Sigma Aldrich (MO, USA). High purity grades (HPLC) of chloroform (CHCl_3 , 99.8%), dichloromethane (DCM, $> 99.9\%$), N,N-Dimethylformamide (DMF, $> 99.9\%$) and methanol (MeOH, 99.9%) were obtained from Samchun Pure Chemical Co., Ltd. (South Korea) while extra pure tert-butanol (*t*-BuOH, 99.5%) and anhydrous magnesium sulfate (MgSO_4 , $> 99\%$) were from Daejung Chemicals and Metals Co., Ltd. (South Korea). Reagents catechol ($\geq 99\%$), epichlorohydrin ($> 99\%$), lithium hydroxide (LiOH , $\geq 98\%$), iodomethane (CH_3I , 99.5%) and sodium hydride (60% NaH in mineral oil) were acquired from Sigma Aldrich (MO, USA). Sodium hydroxide (NaOH , $> 97\%$) and sodium carbonate (Na_2CO_3 , 99.95% extra pure anhydrous) were purchased from Acros Organics (NJ, USA). All compounds for crown ether synthesis were used without further purification.

Polymeric binder PVA (98-99% hydrolyzed, average MW = 85,000-124,000 g mole⁻¹) and glutaraldehyde crosslinker (grade II, 25% in H_2O) were purchased from Sigma-Aldrich (MO, USA). Polyoxyethyleneoctyl phenyl ether (Triton X-100[®]) was from Acros Organics (USA). High purity acetone was purchased from Samchun Pure Chemicals Co., Ltd. (South Korea). Hydrochloric (HCl , RHM 35-37%) and nitric acid (HNO_3 RHM 60%) were supplied by Junsei Chemical Co., Ltd. (Japan). HCl was used as crosslinking catalyst and as stripping agent for the desorption of metal ions in CE/PVA MFs. Meanwhile, HNO_3 was used in acid digestion pre-treatment for elemental analysis. Lithium hydroxide (LiOH $\geq 98\%$) from Sigma-Aldrich (MO, USA) and lithium chloride (LiCl $\geq 98\%$) from Fluka (Switzerland) were used for the preparation of simulated Li^+ solutions for adsorption experiments. Real sample of seawater collected from Pyeongtaek, South Korea was spiked with Li^+ and used for selectivity experiments.

CE diol synthesis protocol

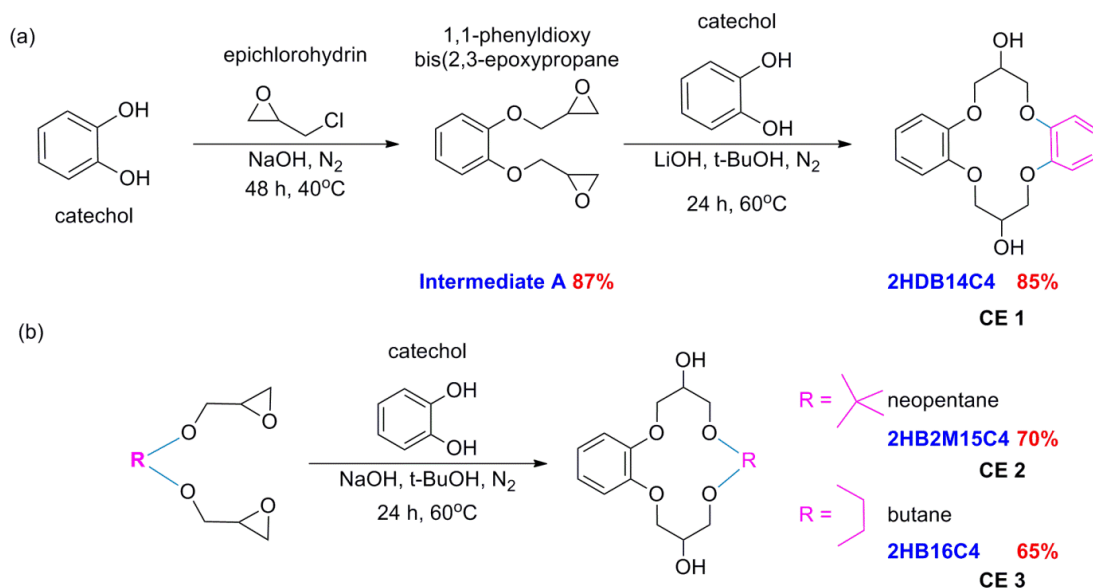


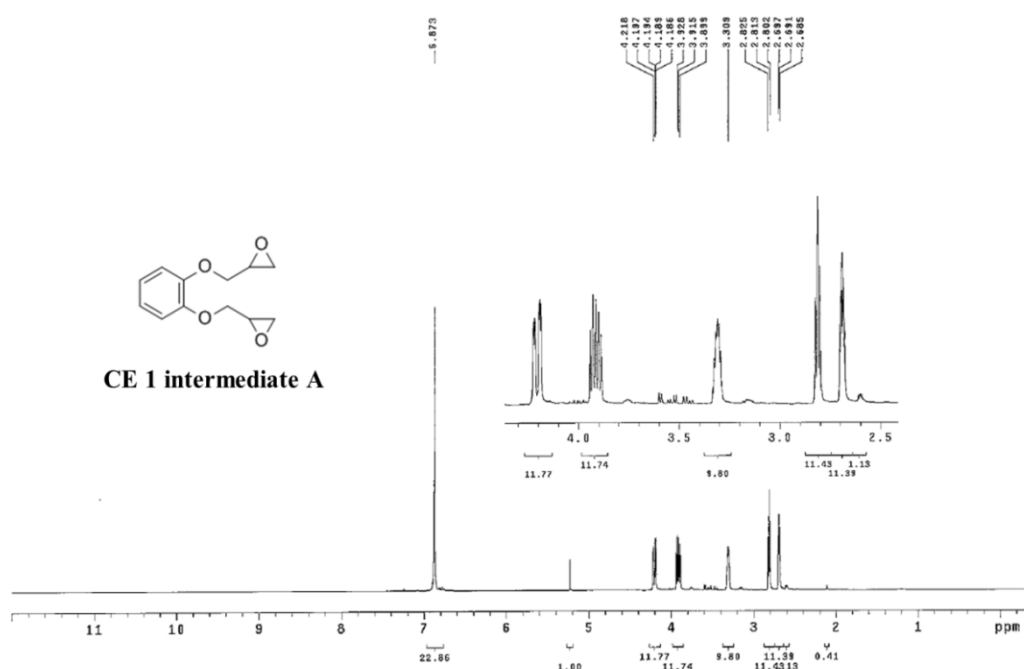
Figure S1. Synthesis scheme of CE diols. (a) 2-step preparation of CE 1 via intermediate A; (b) intermolecular cyclization of various bis-epoxides with catechol for CE 2 and CE 3.

The bis-epoxide intermediate A (1,1-phenyldioxy bis(2,3-epoxypropane)) for CE 1 (2HDB14C4) was obtained from the reaction of (0.1 mol) catechol and (4 equiv., 0.4 mol) epichlorohydrin in the presence of NaOH (0.4 mL, 10 N) under N₂ blanket at 40°C for 48 h (Figure S1a).¹ After cooling, NaOH (42 mL, 5 N) saturated with Na₂CO₃ was added and the mixture was stirred vigorously at room temperature for 20 h. The aqueous layer was extracted twice with CHCl₃ and the combined organic layers were washed and concentrated. The crude product was purified via silica gel column chromatography using DCM as eluent which afforded 87% yield. Meanwhile, bis-epoxides for CE 2 (2HB2M15C4) and CE 3 (2HB16C4) were commercially available and used as received.

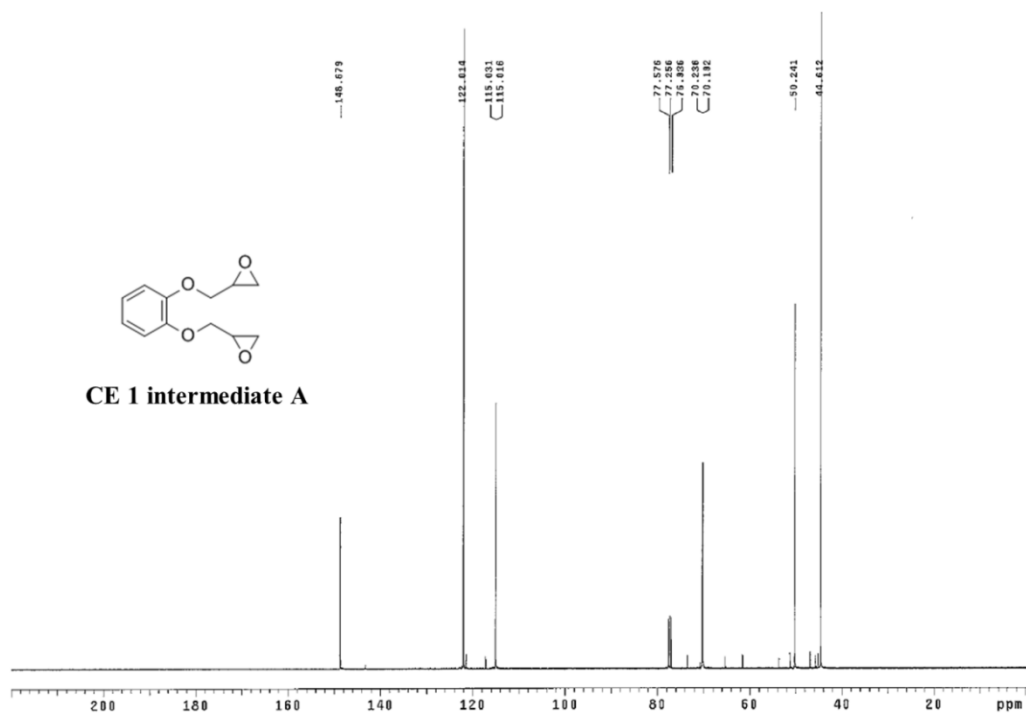
Cyclization of CE diols (Figure S1a, S1b) was performed via reaction of catechol with respective bis-epoxide upon its intramolecular ring opening.^{2,3} Ring closures for CE diols were metal ion template-assisted using metal hydroxides (LiOH or NaOH). Briefly, catechol (5 mmol) and appropriate metal hydroxide (2 equiv., 10 mmol) were dissolved in *t*-BuOH (50 mL) at 60°C under N₂ blanket. Upon complete dissolution, respective bis-epoxide intermediate (1 equiv., 5 mmol) was added within 1 h and the reaction was continuously stirred for 24 h at 60°C. After the reaction, the solvent was evaporated *in vacuo* and the residue was dissolved in CHCl₃. The organic layer was washed with 0.5 N NaOH and finally with water. The water layers were back-extracted with CHCl₃, and the combined CHCl₃ layers were dried over MgSO₄, filtered and evaporated *in vacuo*. Crude products were dissolved in CHCl₃ and purified using silica gel (Merck, 0.035-0.070 mm, 60Å) chromatography with a short alumina (Al₂O₃, Brockman activity I) bed on top (5:1 v/v SiO₂-Al₂O₃) using CHCl₃/MeOH as eluent.

¹H/¹³C NMR spectra of all products are provided as supplementary Figures S2-S5 whereas FTIR spectra of all CE diols were shown in Figure 2 of the main article.

¹H and ¹³C NMR spectra of CE diols

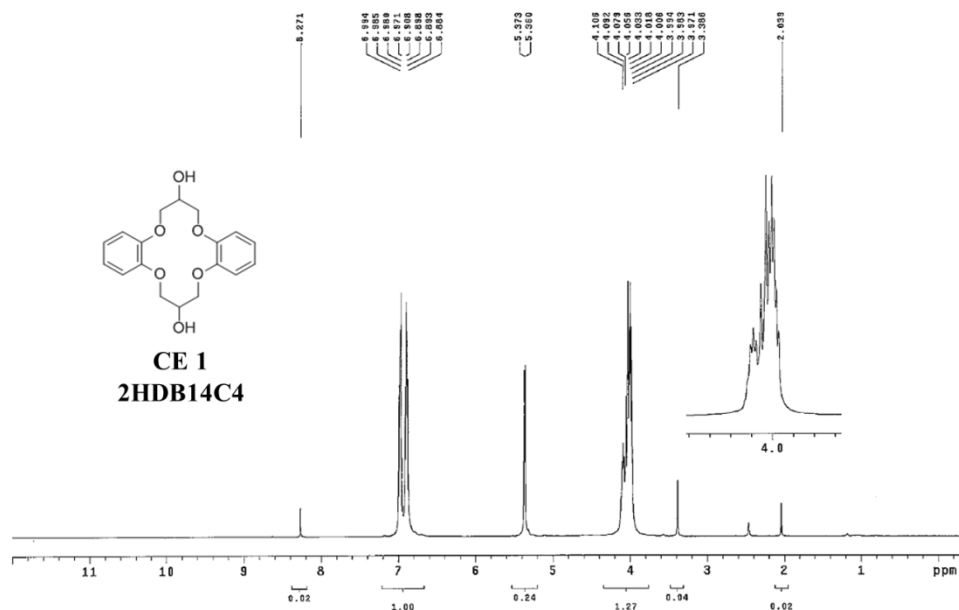


¹H NMR (CDCl₃, 400 MHz): (δ, ppm) 2.68-2.70 (m, 2 H, -CH₂-), 2.80-2.83 (m, 2 H, -CH₂-), 3.30-3.32 (m, 2H, -CH-), 3.89-3.94 (m, 2H, -CH-), 4.19-4.23 (m, 4H, -CH₂-), 6.87 (m, 4H, ArH).

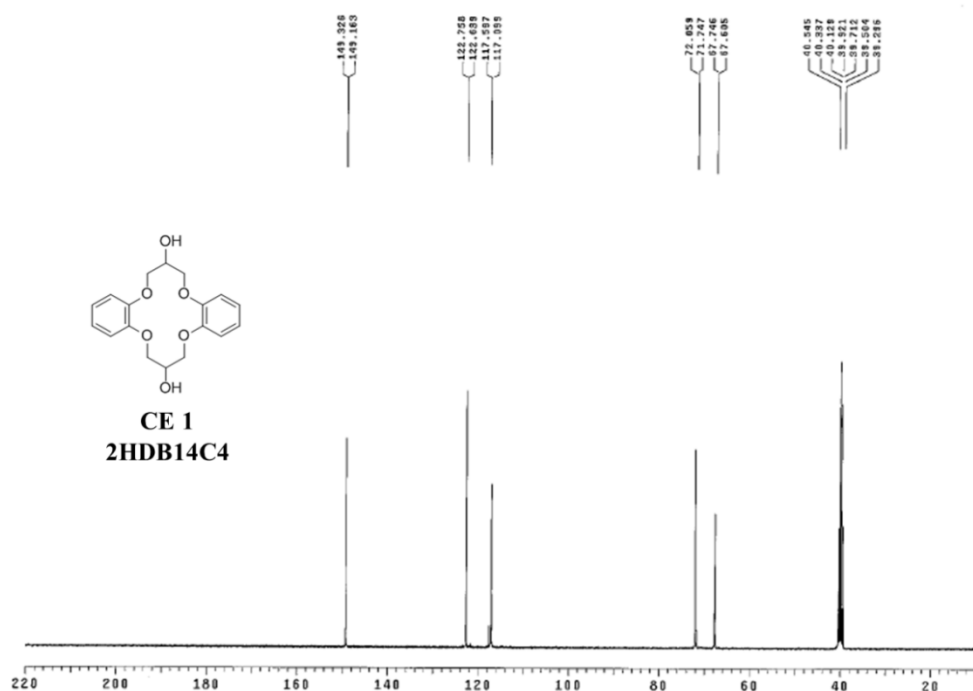


¹³C NMR (CDCl₃, 100 MHz): (δ, ppm) 44.61, 50.24, 70.19, 70.24, 115.02, 115.03, 112.01, 148.68

Figure S2. ¹H and ¹³C NMR spectra of CE 1 intermediate: 1,1-phenyldioxy-bis(2,3-epoxypropane) denoted as CE 1 intermediate A.

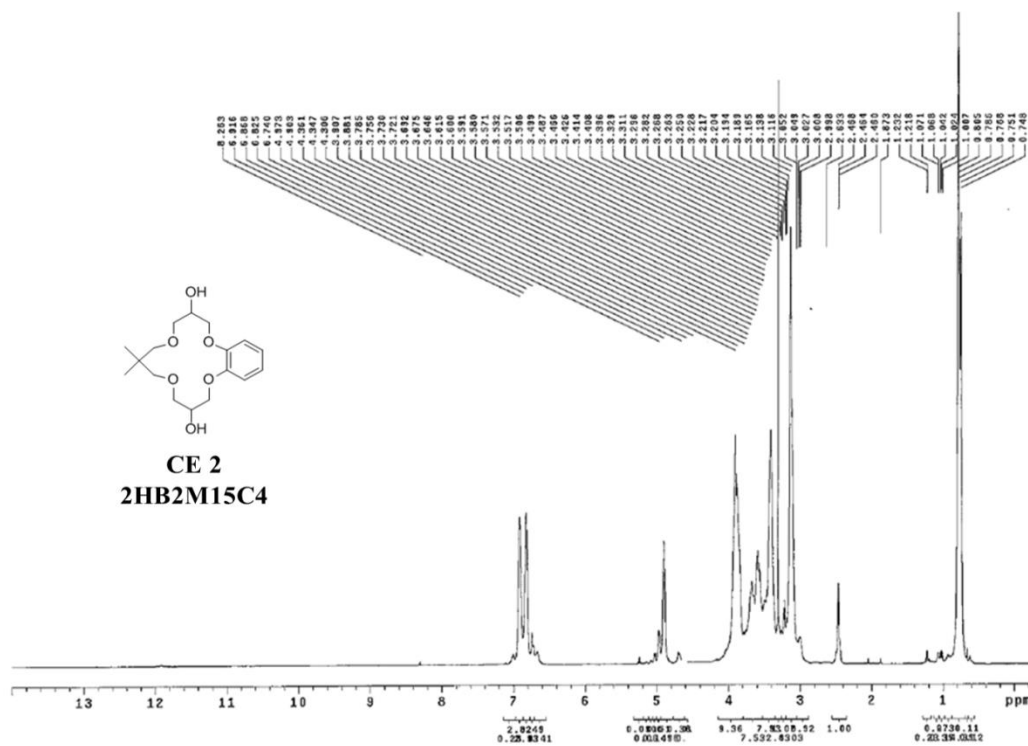


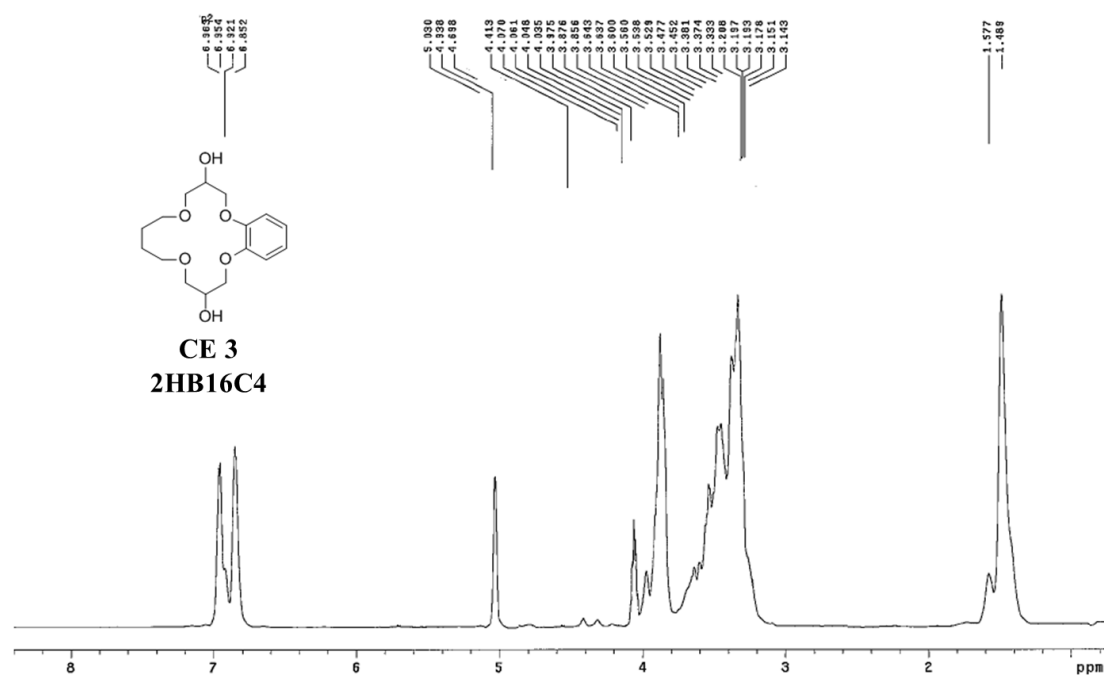
¹H NMR (DMSO-D₆, 400 MHz): (δ, ppm) 1.07 (s, 6 H, 4 -CH₃), 1.09 (s, 6 H, 4 -CH₃), 3.39-3.44 (m, 2 H, -O-CH₂-), 3.64-3.68 (m, 2 H, -O-CH₂-), 3.76-3.82 (m, 4 H, 2 -CH-, -O-CH₂-), 3.89-3.94 (m, 2 H, -O-CH₂-), 4.82 (s, 1H, -OH), 4.83 (s, 1H, -OH), 6.87-6.90 (m, 2H, Ar-H), 6.95-6.98 (m, 2H, Ar-H).



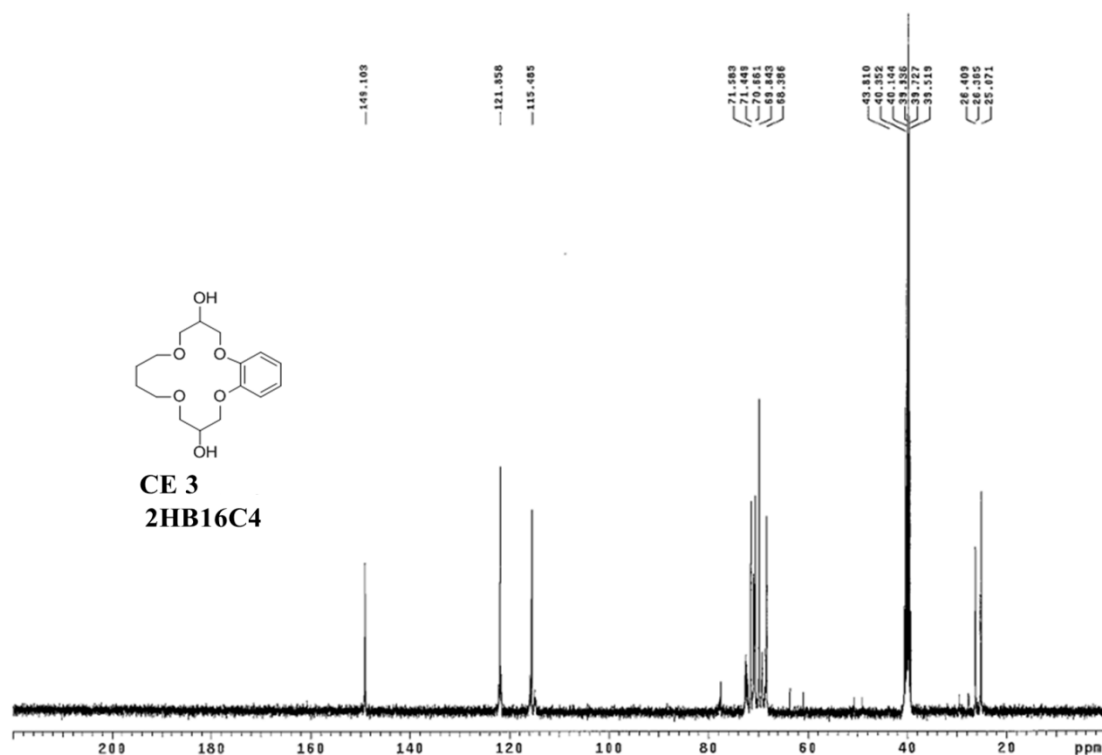
¹³C NMR (DMSO-D₆, 100 MHz): (δ, ppm) 67.61, 67.75, 71.75, 72.06, 117.10, 117.51, 122.64, 122.76, 149.16, 149.33

Figure S3. ¹H and ¹³C NMR spectra of CE 1: 6,7,8,15,16,17-hexahydrodibenzo[1,4,8,11]tetraoxacyclotetradecine-7,16-diol denoted as **2HDB14C4**.





^1H NMR (400 MHz, CDCl_3) δ (ppm): 1.49 (s, 4 H); 3.14-3.64 (m, 10H), 3.85-4.36 (m, 4H), 4.94 (b, 2H), 6.85-6.96 (m, 4H).



^{13}C NMR (100 MHz, CDCl_3): δ (ppm) 25.07, 68.39, 69.84, 70.66, 71.45, 71.58, 115.49, 121.86, 149.10.

Figure S5. ^1H and ^{13}C NMR spectra of CE 3: 2,3,4,6,7,8,9,11,12,13-decahydrobenzo[1,4,8,13] tetraoxacyclohexadecine-3,12-diol denoted as **2HB16C4**.

Electrospinning conditions

Table S1. Electrospinning conditions for the fabrication of MF adsorbents.

Parameters	Values
Dope solution	
Polymer	PVA
Polymer concentration	9 wt%
Solvent	Water
Organic adsorbents	2HDB14C4, 2HB2M15C4, 2HB16C4
CE loading in PVA	50 wt%
Electrospinning conditions	
Dope solution volume (mL)	12
Syringe with a needle	$\varnothing_{\text{inner}} = 0.51 \text{ mm}$
Syringe pump speed (mL hr ⁻¹)	2
Voltage (kV)	24-26
Needle inner diameter (mm)	0.51
Needle tip-collector distance (mm)	120
Collector	Drum roll type
Collector rotation speed (RPM)	500
Nanofiber drying temperature (°C)	50
Nanofiber drying time (h)	5

Synthesis of Methylated CEs (mCEs) for control MF samples

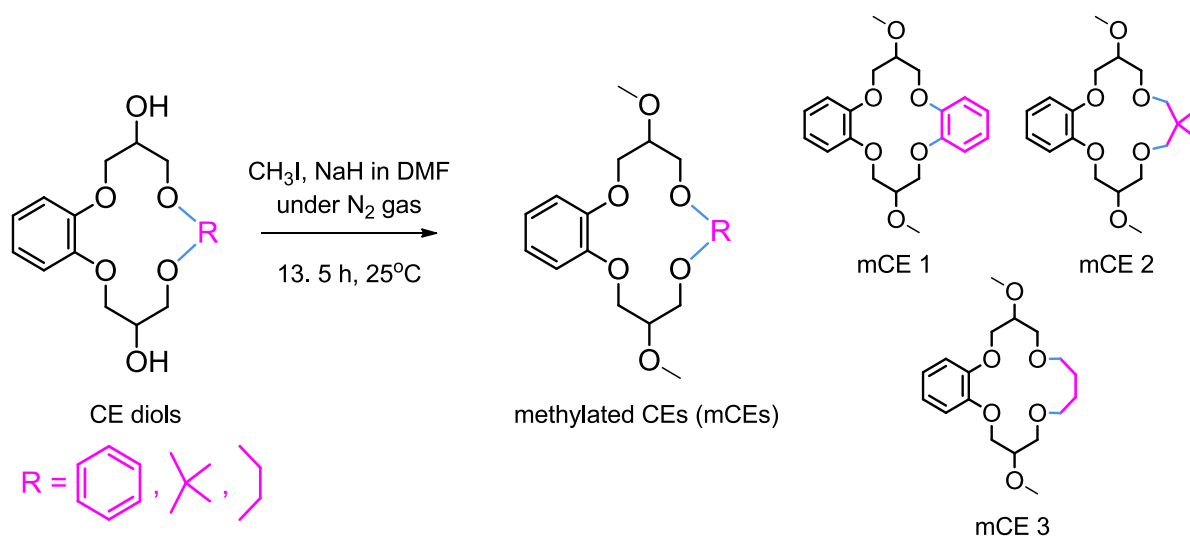


Figure S6. Synthesis scheme of methylated CEs via etherification.

Methylated CEs (mCE) were synthesized by etherification of CE diols with iodomethane (CH_3I). Each CE diol (4g, 12 mmol) was dissolved in 10 mL anhydrous DMF. The solution was added slowly in 100 mL three neck RBF containing NaH (3 eq., 36 mmol) dispersed in 20 mL anhydrous DMF under N_2 gas. The reaction was stirred for 1 h before slowly adding CH_3I (8 eq., 96 mmol), which was dissolved in 10 mL anhydrous DMF, within 30 min. The reaction was continuously stirred at room temperature for another 12 h before quenching with water and DCM (200 mL). The reaction product was washed repeatedly with water (~2 L) to remove DMF. The organic phase was dried over MgSO_4 and reduced under vacuum. The crude oil was purified by silica gel chromatography using CHCl_3 as eluent to afford the corresponding mCEs in excellent yields (mCE 1, 4.1 g, **92% yield**; mCE 2, 3.9 g, **90% yield**; mCE 3, 3.5 g, **85% yield**).

Characterization results of mCE compounds

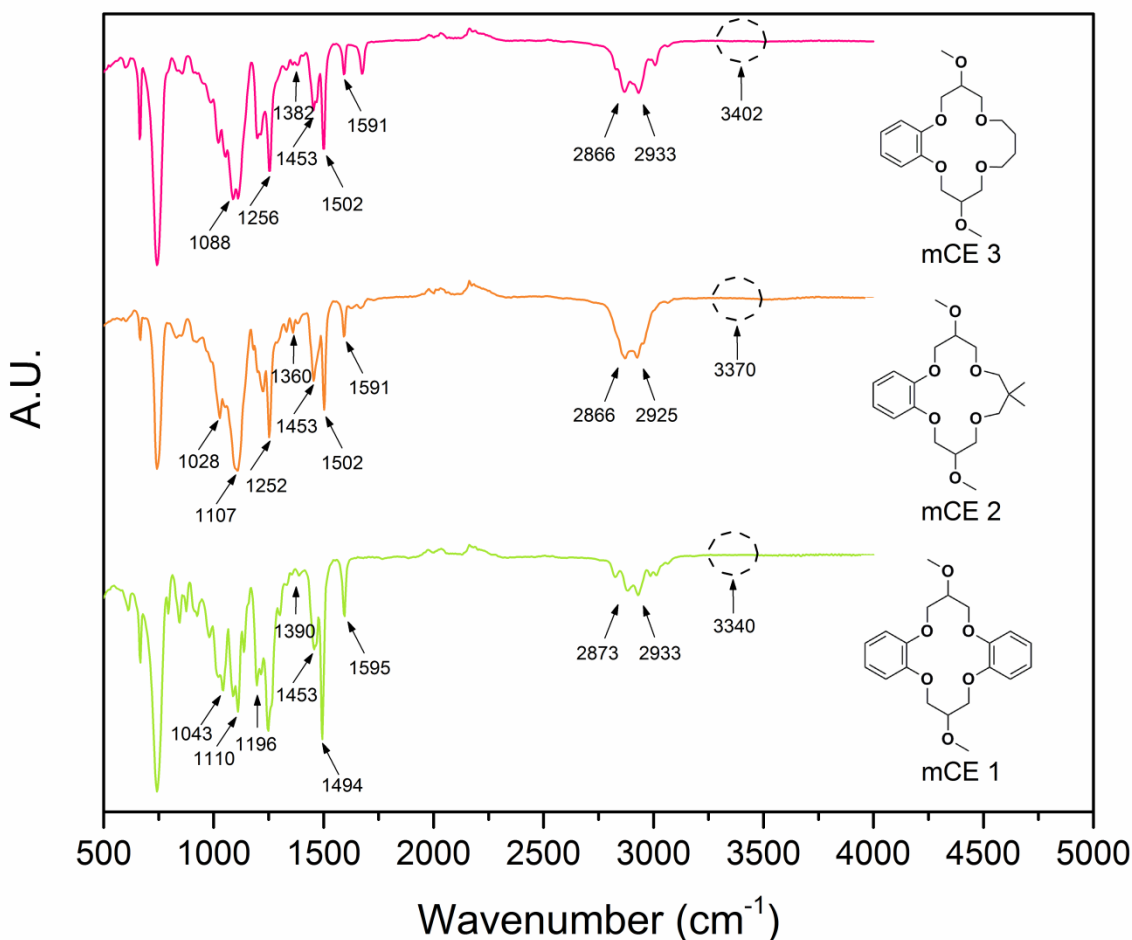


Figure S7. FTIR spectra of methylated CEs (mCE 1 – 3).

Similar to the CE diols (Figure 3b), methylated CEs (mCEs) exhibited characteristic FTIR peaks from the C-H stretching ($2933\text{--}2866\text{ cm}^{-1}$)^{4,5} and C-H bending ($1390\text{--}1360\text{ cm}^{-1}$) of the etherified CH_3 groups and CE rings, from the C=C stretching of benzene ($1594\text{--}1452\text{ cm}^{-1}$)⁶ and from the C-O-C ether stretching of the rings ($1257\text{--}1032\text{ cm}^{-1}$).⁷ FTIR also reflected the main difference between the CE diols and mCEs. The absence of vibrational O-H peaks ($3402\text{--}3340\text{ cm}^{-1}$) in mCE samples strongly indicates successful etherification of CE diols with CH_3 .

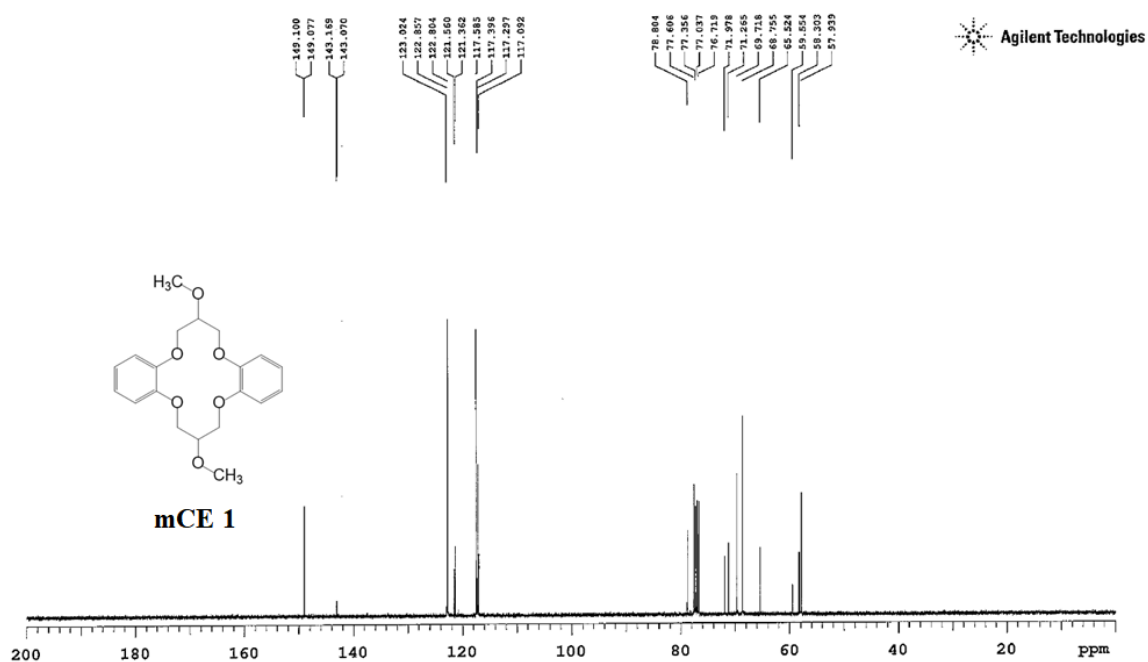
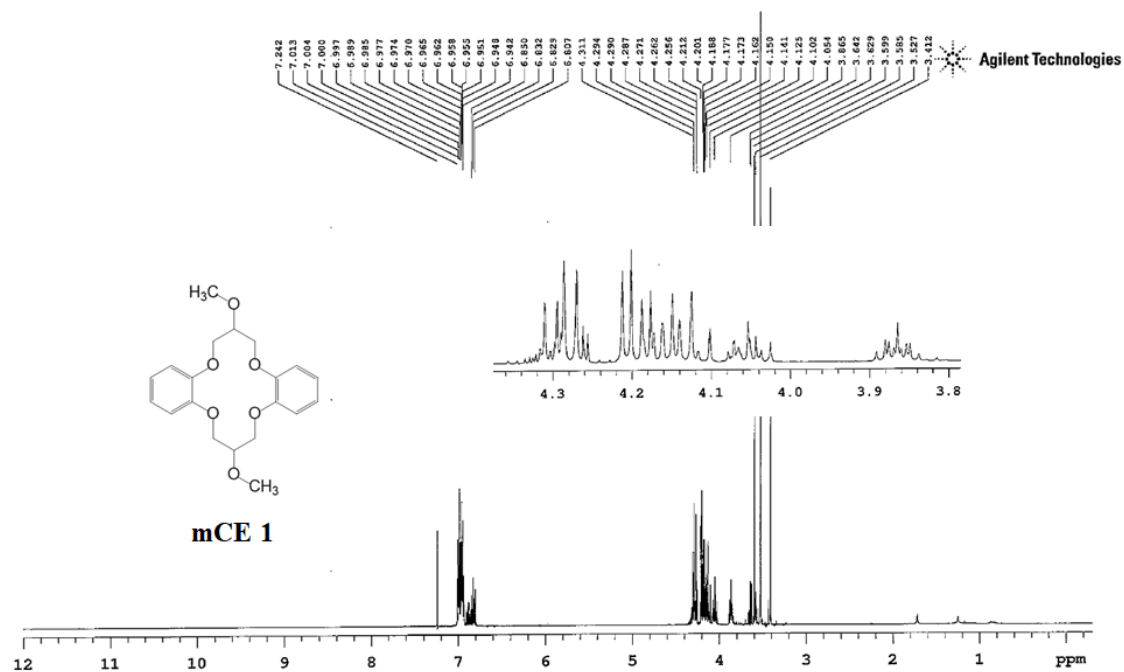


Figure S8. ¹H and ¹³C NMR spectra of **mCE 1**: 7,16-dimethoxy-6,7,8,15,16,17-hexahydrodibenzo[b,i][1,4,8,11]tetraoxacyclotetradecine.

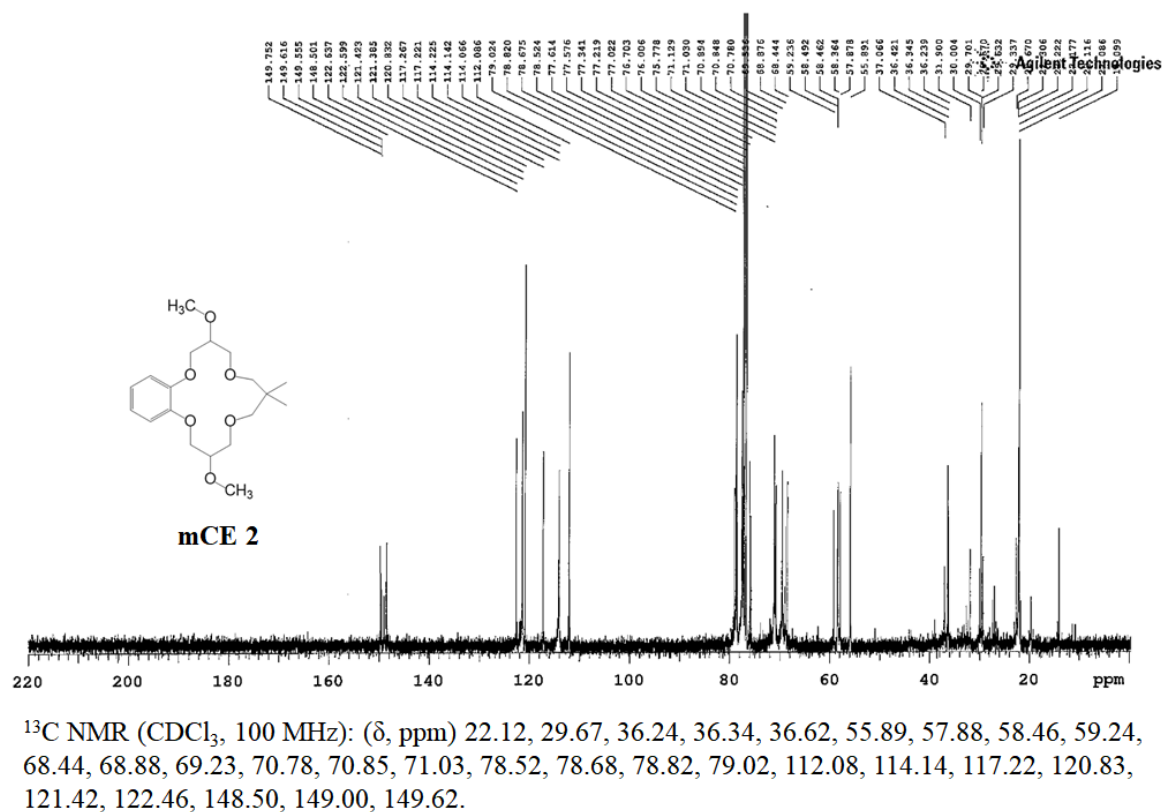
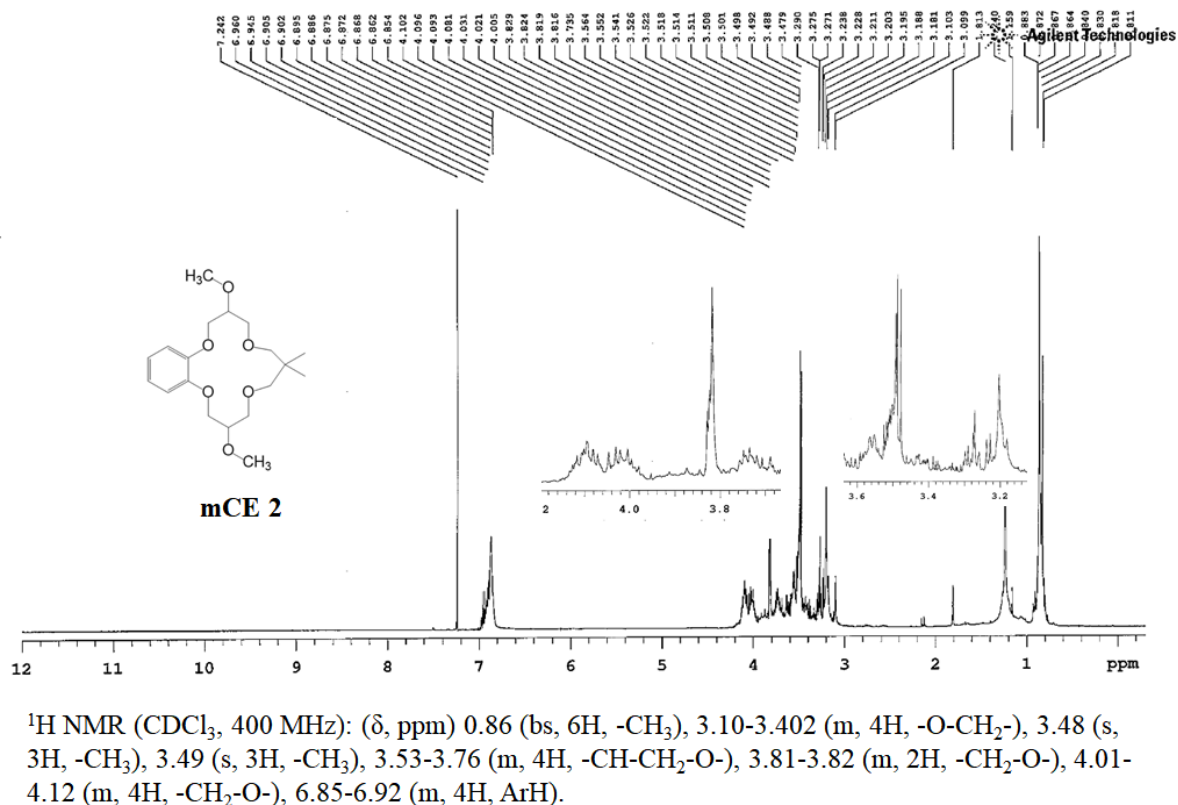


Figure S9. ^1H and ^{13}C NMR spectra of **mCE 2**: 3,11-dimethoxy-7,7-dimethyl-3,4,6,7,8,10,11,12-octahydro-2H-benzo[b][1,4,8,12]tetraoxacyclopentadecine.

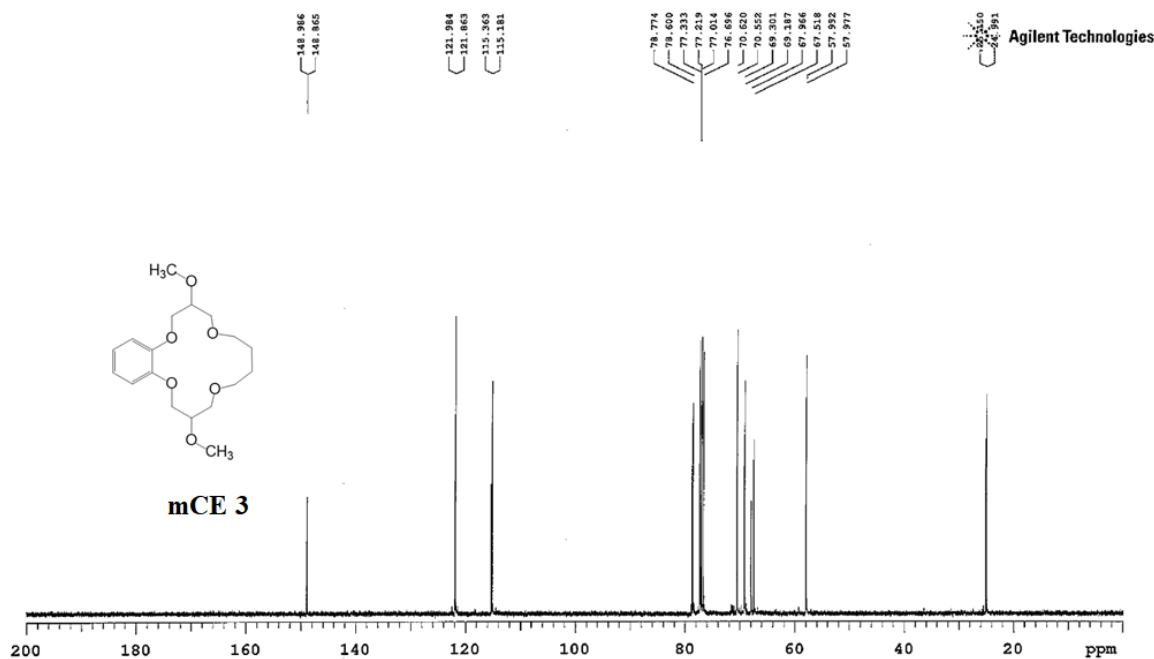
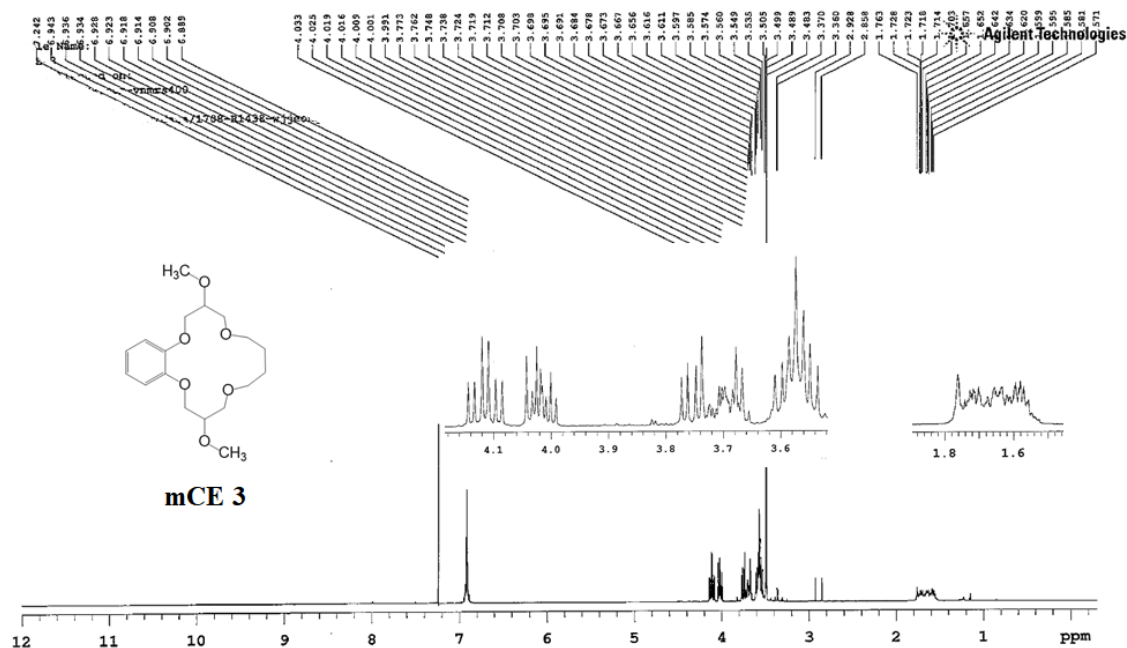


Figure S10. ¹H and ¹³C NMR spectra of **mCE 3**: 3,12-dimethoxy-2,3,4,6,7,8,9,11,12,13-decahydrobenzo[b][1,4,8,13]tetraoxacyclohexadecine.

Calculations for MF stability tests

Table S2 (p. S19) summarizes the equations used for the stability tests performed on crosslinked CE/PVA and control mCE/PVA MFs. In Table S2, w_1 = weight of a pristine electrospun MF sample; weight fractions of CE (f_{CE}) and PVA (f_{PVA}) are based on 50 wt% CE loading with respect to PVA amount. For example, 1 g of PVA in dope is added with 0.5 g of CE diol thus $f_{PVA} \cong 1 \text{ g}/1.5 \text{ g} \cong 0.667$ whereas $f_{CE} \cong 1 - 0.667 = 0.333$. Thus, for any sample with w_1 , the mass of CE is $m_{CE} = f_{CE} \times w_1$ and PVA is $m_{PVA} = (1 - f_{CE}) \times w_1$. After aerosol crosslinking, weight of the unwashed aerosol crosslinked MF (w_2) was determined. Before the test, the m_{PVA} and m_{CE} would still be the same as in w_1 . Thus, the weight gain ($w_2 - w_1$) could be the GA component which crosslinked the MF (m_{GA}).

After careful drying of the samples from the elution test (section 2.5 main article), the MFs are re-weighed as w_3 . Thus, total % MF mass loss = $(w_3 - w_2)/w_2 \times 100$. The CEs eluted from the fibers (m_{CE_loss}) were determined by quantifying the CE concentration $[CE]_{UV-Vis}$ in the ($V = 50 \text{ mL}$) eluent, using UV-VIS spectrophotometry (section 2.8, main article). Dividing m_{CE_loss} with m_{CE} estimates the % CE loss in the MF sample. The eluents were also analyzed for total organic carbon (TOC) concentration (section 2.8 main article) which is the total carbons for PVA + CE components, $[C]_{TOC} = [PVA]_C + [CE]_C$. No GA was eluted from the MF as indicated by the clean UV-Vis spectra of the eluents (Fig. S15); only eluted CEs were detected. The unreacted GAs were efficiently removed when the MFs were vacuum-dried at 50°C after the crosslinking step.⁸ Thus, the mass of PVA lost (m_{PVA_loss}) was determined using $[C]_{TOC} - [CE]_C$. Conversions of CE and PVA concentrations as C mg L^{-1} ($[CE]_C$ and $[PVA]_C$) and vice versa were performed using the carbon mass fractions in CE diols (f_{C-CE}) and PVA (f_{C-PVA}). Dividing m_{PVA_loss} with m_{PVA} estimates the % PVA loss in the MF sample.

Actual composition of MFs used for adsorption studies

Calculations for the elution tests (Table S2) can also be used to determine the actual mass fractions of components in washed MF samples. After pre-washing, the washing solutions of MFs were analyzed for eluted CE and PVA as described above. After drying the MF samples, prior to adsorption experiments, the final weight m_{MF} is in fact equivalent to w_3 ($m_{MF} = w_3$) as described in Table S2. So actual mass of CE in the washed MF is equal to $m'_{CE} = m_{CE} - m_{CE_loss}$ whereas actual PVA in the washed MF is equal to $m'_{PVA} = m_{PVA} - m_{PVA_loss}$. Meanwhile, $m_{GA} = w_3 - m'_{CE} - m'_{PVA}$ which is almost the same as $w_2 - w_1$ (Table S2). Thus, actual mass fractions of each component $f'_{CE} = m'_{CE}/m_{MF}$, $f'_{PVA} = m'_{PVA}/m_{MF}$, and $f'_{GA} = m_{GA}/m_{MF}$ can be known (see Table S2) for washed MFs used for adsorption studies.

Using this experimentally determined mass fractions (f'_{CE} , f'_{PVA} , f'_{GA}), the adsorption contribution of each component can be known according to the modified adsorption model.⁹

$$q_e = q_{CE} \cdot f'_{CE} + q_{GA/PVA} \cdot (1 - f'_{CE})$$

To determine the adsorption capacity of the CE component (q_{CE}) from the experimental adsorption results, the equation above can be re-arranged as shown below:

$$q_{CE} = \frac{q_e - [q_{GA/PVA} \cdot (1 - f'_{CE})]}{f'_{CE}}$$

Table S2. List of equations used for the stability tests and actual MF composition determination.

Fresh electrospun MFs	Aerosol GA crosslinked MFs	MFs after stability test
$w_1 = m_{CE} + m_{PVA}$	$w_2 = m_{CE} + m_{PVA} + m_{GA}$	$w_3 = (m_{CE} - m_{CE_loss}) + (m_{PVA} - m_{PVA_loss}) + m_{GA}$ $= m'_{CE} + m'_{PVA} + m_{GA}$
For 50 wt% CE loading in dope:		$\% MF\ mass\ loss = \frac{w_2 - w_3}{w_2} \times 100$
If $w_{CE} \cong 0.5$ g, then $w_{PVA} \cong 1.0$ g		$m_{CE_loss} = [CE]_{UV-Vis} \times V_{eluent}$
$f_{CE} = \frac{w_{CE}}{w_{CE} + w_{PVA}} \cong 0.333$		$\% CE\ loss = \frac{[CE]_{UV-Vis} \times V_{eluent}}{m_{CE}} \times 100$
$f_{PVA} = (1 - \frac{w_{CE}}{w_{CE} + w_{PVA}}) \cong 0.667$		$m_{PVA_loss} = \frac{([C]_{TOC} - [CE]_C) \times V_{eluent}}{f_{C-PVA}} = [PVA] \times V_{eluent}$
		$\% PVA\ loss = \frac{[PVA] \times V_{eluent}}{m_{PVA}} \times 100$
		Conversions: $[C]_{TOC} = [PVA]_c + [CE]_c$ $[PVA]_c = [PVA] \times f_{C-PVA}$ $[CE]_c = [CE]_{UV-Vis} \times f_{C-CE}$
Component masses in uncrosslinked MF sample:		Final component masses of washed MF samples:
$m_{CE} = f_{CE} \times w_1$		$m_{GA} = w_3 - m'_{CE} - m'_{PVA} \cong w_3 - w_2$
$m_{PVA} = f_{PVA} \times w_1$		$f'_{GA} = \frac{m_{GA}}{w_3}; f'_{PVA} = \frac{m'_{PVA}}{w_3}; f'_{CE} = \frac{m'_{CE}}{w_3}$

Calibration curves for PVA and CE concentrations in elution tests

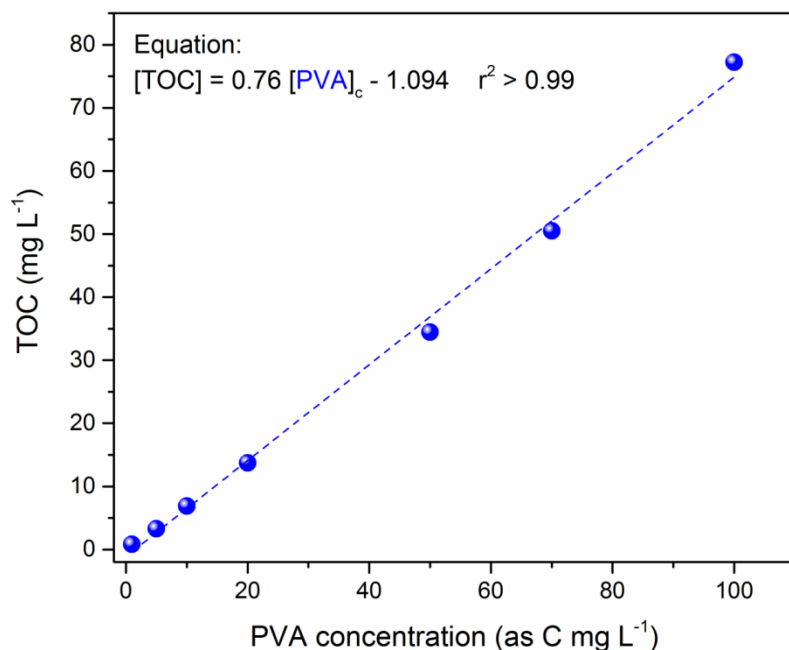


Figure S11. Calibration curve for PVA [as C] via TOC analysis.

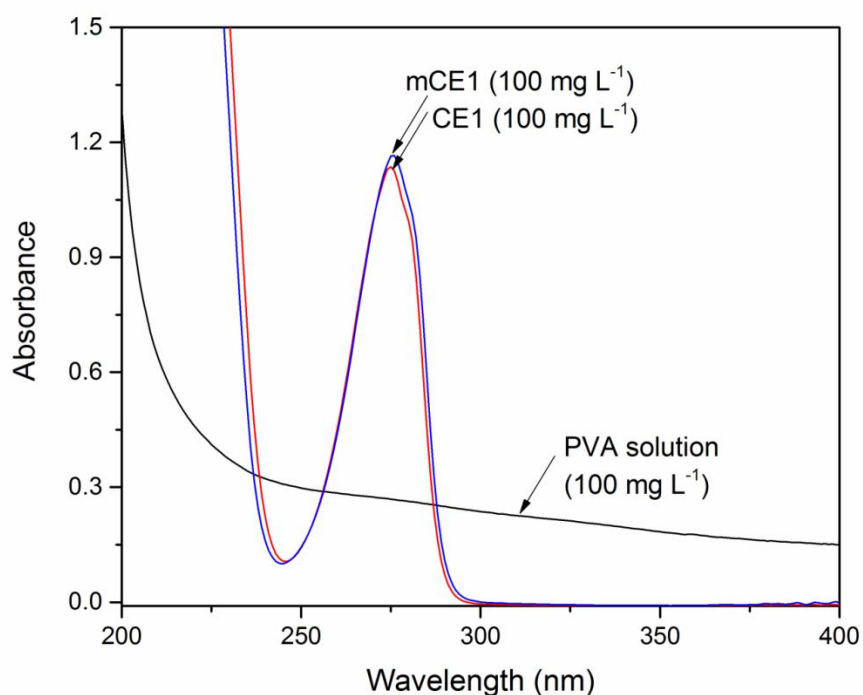


Figure S12. UV-Vis spectra of mCEs and CE diols with no interference from PVA. This method was used to selectively quantify the CEs dissolved in water (pH = 8) during the MF adsorbent stability test.

Calibration curves for PVA and CE concentrations in elution tests

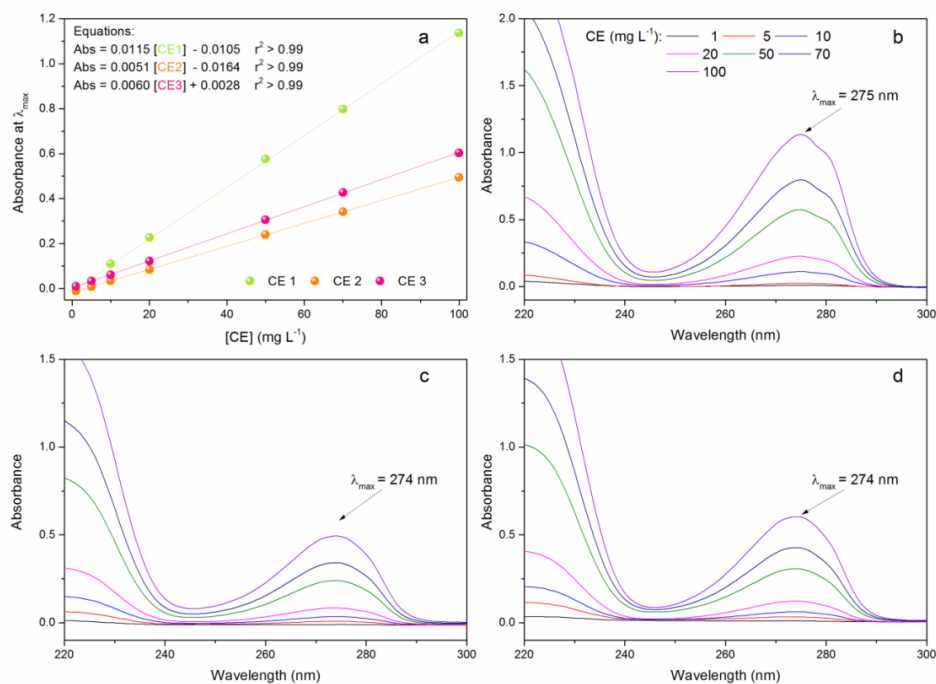


Figure S13. Constructed standard curves for (a) CE diols using UV-Vis spectrophotometry (5 – 100 mg L⁻¹). The maximum absorbances at λ_{max} were recorded for (b) CE 1, (c) CE 2, and (d) CE 3.

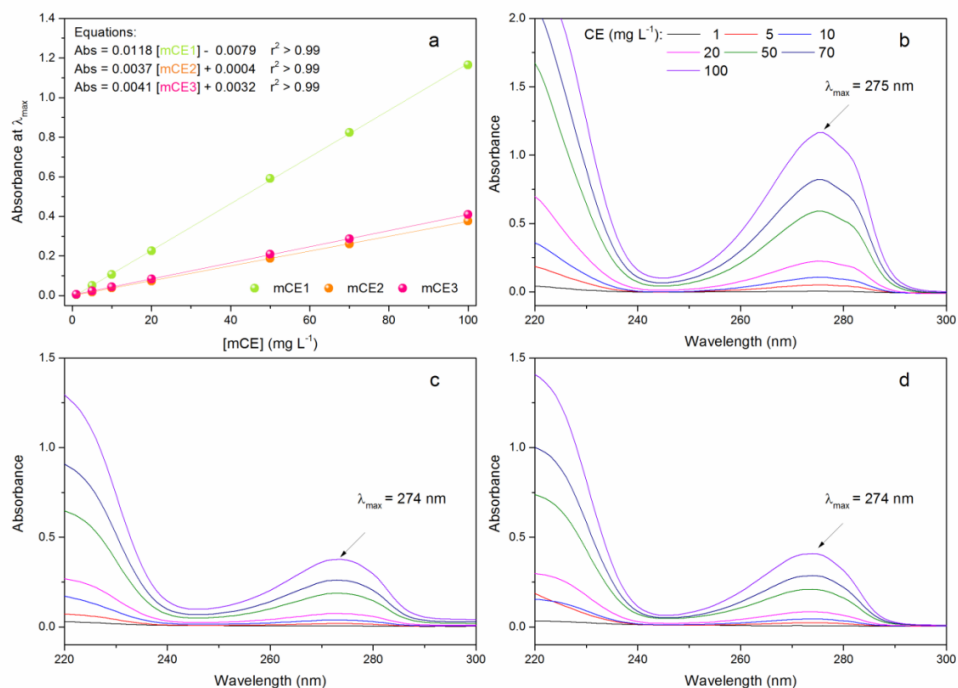


Figure S14. Constructed standard curves for (a) methylated CEs (mCEs) using UV-Vis spectrophotometry (5 – 100 mg L⁻¹). The maximum absorbances at λ_{max} were recorded for (b) mCE 1, (c) mCE 2, and (d) mCE 3.

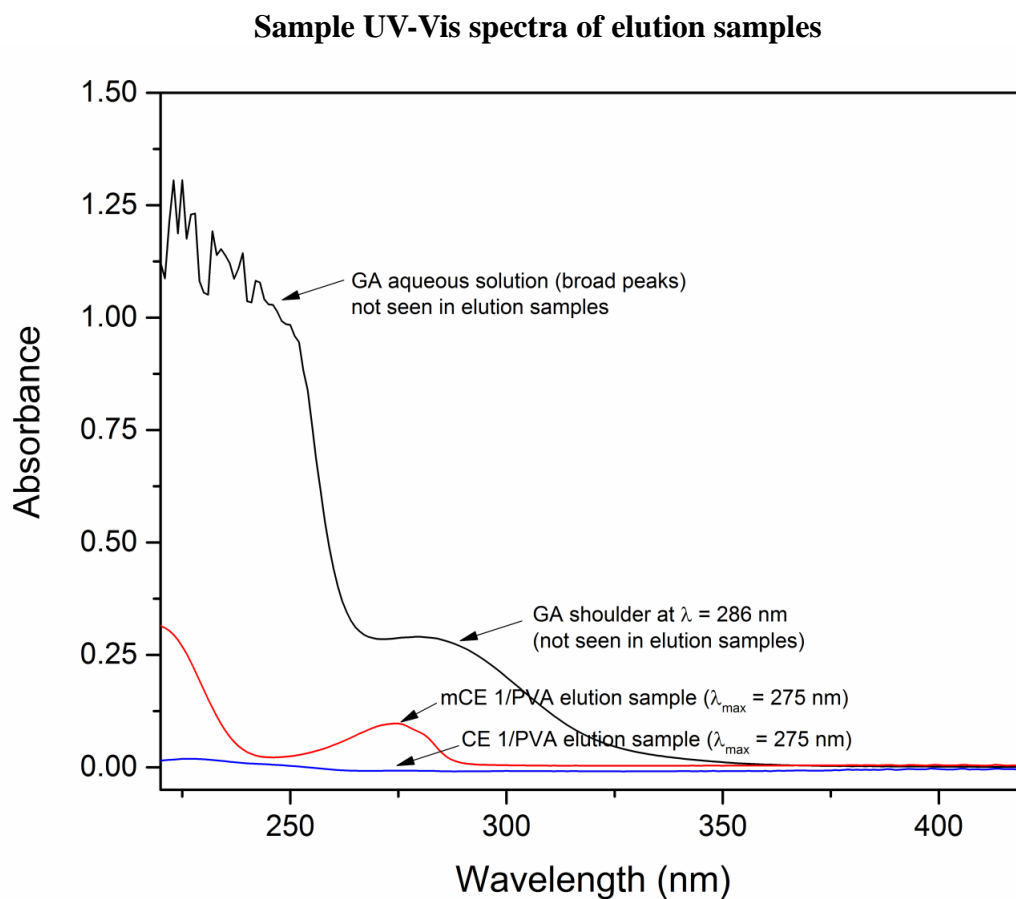


Figure S15. Sample UV-Vis spectra of eluent samples from CE/PVA and mCE/PVA MFs. A spectrum for GA aqueous solution is overlaid.

Elution samples of CE/PVA and mCE/PVA did not contain characteristic peaks of GA, suggesting that no residual GA was eluted from the MFs. Residual GA is typically removed (evaporation) during MF crosslinking and vacuum-drying at 50°C.⁸

Table S3. Integrated FTIR peaks and corresponding ratios.

CE 1	Area	Height	Centroid	CE 1/GA	Area	Height	Centroid	I_p
C-H doublet	1184.63	10.41	2874.88	C-H doublet	1852.33	15.65	2889.14	1.56
O-H	4031.29	14.31	3382.11	O-H	3903.55	11.98	3382.17	0.97
C=O GA residual	-	-	-	C=O GA residual	910.26	20.36	1700.59	-
CE 2				CE 2/GA				
C-H doublet	2796.58	22.94	2888.90	C-H doublet	3011.47	24.20	2887.15	1.08
O-H	3908.29	12.42	3388.60	O-H	1937.85	7.27	3409.91	0.50
C=O GA residual	-	-	-	C=O GA residual	319.77	5.18	1711.13	-
CE 3				CE 3/GA				
C-H doublet	3487.85	29.29	2882.96	C-H doublet	3774.61	29.38	2879.96	1.08
O-H	4862.61	13.25	3386.38	O-H	2286.84	8.42	3413.34	0.47
C=O GA residual	-	-	-	C=O GA residual	95.49	4.38	1722.53	-

Prior integration, baseline correction (2nd derivative) was performed in all FTIR spectra. After GA crosslinking, all samples had reduced OH groups ($I_p < 1$) and increased C-H stretching ($I_p > 1$). These results are indicative of GA crosslinking which involves OH consumption from the diols and incorporation of GA alkyl chains in CE/GA samples.^{5,8} Moreover, broadened peaks at 1034 cm⁻¹ (CE 1/GA), 1103 cm⁻¹ (CE 2/GA) and 1106 cm⁻¹ (CE 3/GA) are strong indications of acetal group formation.^{4,5,10} These results confirm the reactivity of CE diols with GA, which is critical for the creation of CE-GA-PVA linkages. If the diols are to be ranked according to their GA reactivity, CE 2 and CE 3 are more reactive than CE 1 as both had higher OH groups consumed at similar extents ($I_p \sim 0.47 - 0.50$). But CE 3 was the most reactive given its lowest content of unreacted GA (C=O peak area of 95.49). This suggests that the differences in CE structures must have affected their GA reactivities. Overall results demonstrate that CE 3, which has the least bulky sub-unit, is the most GA reactive. On the other hand, CE 1 which might have encountered steric hindrances from its benzo groups,¹¹ is the least amenable to GA crosslinking.

Elution test results and actual compositions of MFs used for adsorption experiments

Table S4. Swelling ratio and measurements for the stability test of pure PVA, CE/PVA and mCE/PVA MFs.

Type	Swelling Ratio (<i>S</i>)	w_1 (mg)	m_{CE} (mg)	m_{PVA} (mg)	w_2 (mg)	$[CE]_{UV-vis}$ (mg L ⁻¹)	$[C]$ mg L ⁻¹	$[PVA]$ (mg L ⁻¹)
CE 1/PVA	0.127 ± 0.007	25.05 ± 3.46	8.36 ± 1.16	16.69 ± 2.31	27.00 ± 3.96	0.36 ± 0.17	3.33 ± 0.33	5.67 ± 0.79
CE 2/PVA	0.134 ± 0.011	23.15 ± 0.64	7.77 ± 0.21	15.38 ± 0.42	25.30 ± 1.84	0.85 ± 0.11	4.09 ± 0.17	6.52 ± 0.44
CE 3/PVA	0.132 ± 0.001	26.80 ± 3.25	9.11 ± 1.11	17.69 ± 2.15	29.25 ± 3.04	0.22 ± 0.07	3.33 ± 0.59	6.10 ± 0.59
mCE 1/PVA	0.413 ± 0.185	-	9.52 ± 0.61	19.94 ± 1.23	28.60 ± 1.84	23.35 ± 0.13	70.89 ± 0.19	29.67 ± 0.15
mCE 2/PVA	0.229 ± 0.154	-	8.54 ± 0.54	17.11 ± 1.08	25.70 ± 1.63	59.22 ± 0.38	104.97 ± 0.47	37.07 ± 0.13
mCE 3/PVA	0.231 ± 0.121	-	9.71 ± 0.31	19.44 ± 0.61	29.20 ± 0.92	183.96 ± 9.29	229.99 ± 9.58	63.77 ± 2.11
Pure PVA	0.321 ± 0.036	27.75 ± 2.05	0	27.75 ± 2.05	29.80 ± 1.56	0	3.00 ± 0.32	5.50 ± 0.59

Table S5. Component losses (CE and PVA) during elution tests and the final composition of MF samples used for adsorption experiments.

Type	$m_{loss-CE}$ (mg)	$m_{loss-PVA}$ (mg)	% CE loss	% PVA loss	m_{MF} (mg)	m_{GA} (mg)	f'_{CE}	f'_{PVA}	f'_{GA}
CE 1/PVA	0.018 ± 0.008	0.28 ± 0.04	0.23 ± 0.13	1.70 ± 0.00	26.7 ± 4.0	1.95 ± 0.49	0.313 ± 0.003	0.615 ± 0.006	0.072 ± 0.008
CE 2/PVA	0.042 ± 0.005	0.33 ± 0.02	0.54 ± 0.05	2.12 ± 0.20	24.9 ± 1.8	2.15 ± 1.20	0.311 ± 0.015	0.606 ± 0.027	0.085 ± 0.042
CE 3/PVA	0.011 ± 0.004	0.31 ± 0.03	0.12 ± 0.03	1.73 ± 0.04	29.0 ± 3.0	2.45 ± 0.21	0.313 ± 0.006	0.599 ± 0.012	0.085 ± 0.016
mCE 1/PVA	1.272 ± 0.007	4.99 ± 0.03	13.34 ± 0.79	26.20 ± 1.82	-	-	-	-	-
mCE 2/PVA	2.961 ± 0.019	6.23 ± 0.02	34.73 ± 1.98	36.48 ± 2.19	-	-	-	-	-
mCE 3/PVA	9.198 ± 0.465	10.72 ± 0.35	94.73 ± 1.80	55.12 ± 0.08	-	-	-	-	-
Pure PVA	0	0.28 ± 0.03	0	0.99 ± 0.03	29.5 ± 1.5	2.05 ± 0.49	0	0.929 ± 0.022	0.070 ± 0.020

¹³C CP/MAS NMR results and peak interpretation

Due to the broad peaks of ¹³C CP-MAS NMR spectra (Figure S16-S19), the results were partially resolved and predicted using MestRenova 11.0.2.¹² The identified peaks and assignments were listed in Tables S6-S9. In GA crosslinked pure PVA MF (Figure S16, Table S6), the acetal (1)¹³ and hemi-acetal carbons (2)¹⁴ formed during GA crosslinking were detected. Likewise, α,β -carbons of the PVA chain were evident, which contained either the crosslinked (3,6) or unreacted OH groups (4,5). Same as the peaks assigned for the α,β -carbons of crosslinked GA (6,7), which are located in the most upfield region of the spectrum.

In CE/PVA samples (Figures S17-S19), similar peaks assigned to the unreacted α,β -carbons in the PVA chains (8-12) and α,β -carbons of crosslinked GA (12-15) were also detected. It also affirms the presence of residual GA (a) in CE 1/PVA as initially revealed by the FTIR results (Figure 3c in article). But unlike the FTIR, characteristic peaks of the CE components were visible in the ¹³C CP-MAS NMR. Particularly, the benzyl carbons (1-3) were identified with those bearing ethereal oxygens as the most deshielded (1).¹⁵ The benzyl carbon signals are most remarkable in CE 1/PVA, due to the dibenzo-functionalized CE 1 (Figure S17, Table S7). On the other hand, peaks assigned to the carbon R sub-units in CE 2 and CE 3 were also identified like the tertiary (12) and alkyl carbons (*b*,13) in CE 2/PVA (Figure S18, Table S8), and the butyl carbons (8,14) in CE 3/PVA (Figure S19, Table S9).

The most indicative signals for the CE/GA linkages are those near 70 ppm. By contrast, CE/PVA samples have three resolved peaks (7-9) which were slightly shifted downfield relative to those two (3-4) in pure PVA. Unreacted α -carbons (C-OH) in PVA and CEs were easily identified (9). As an attempt to decouple the α,β -carbon resonances in crosslinked PVA and CEs, the possible linkages were identified using MestRenova® predictor as detailed in SI p. S30.

Analysis of partially resolved peaks reveals that several types of crosslinks might have been formed. As seen in the spectra, Type I involves acetal carbon (5) formation from GA/PVA linkage whereas Type II identifies acetal carbon (4) formation from GA reacted with one OH-CE and one OH-PVA. Meanwhile, another possible form of linkage (III) involves only one OH of CE in GA crosslinking with its other OH group left unreacted. However, current results cannot confirm nor rule out this type of linkage. Hemi-acetal carbons (6) between CE/GA and PVA/GA linkages were also detected (IV).¹⁴

¹³C CP/MAS NMR results

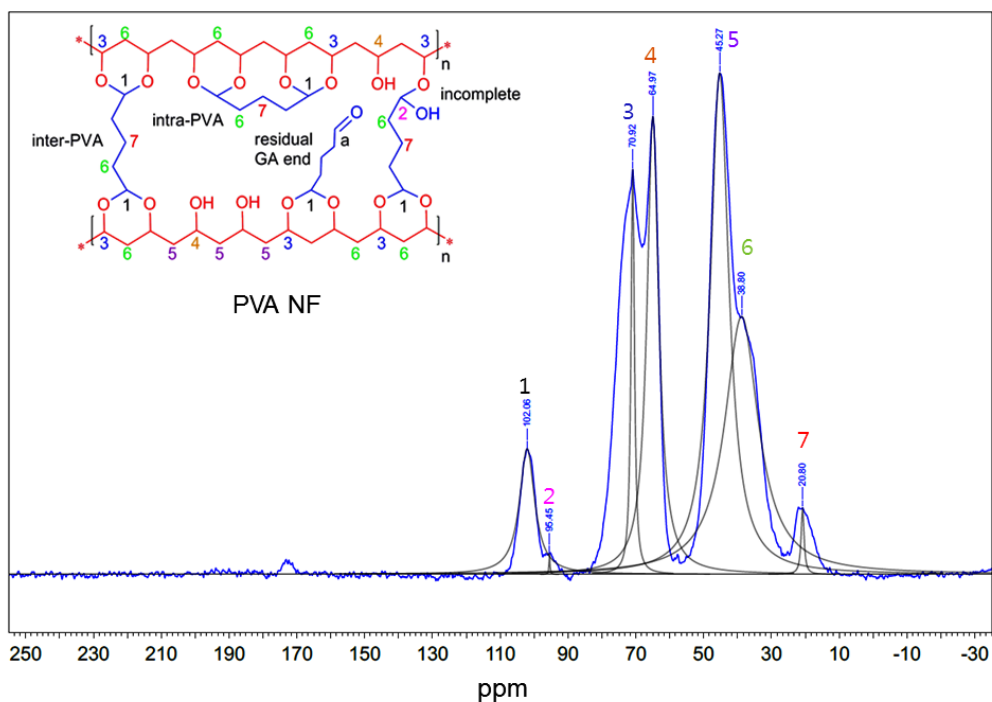


Figure S16. ¹³C CP/MAS NMR of pure PVA MF.

Table S6. Chemical shifts from ¹³C CP/MAS NMR and peak assignments for pure PVA MF.

Crosslink Type	Peak Number	Chemical Shift (δ, ppm)	Assignments
(I)	1	102.06	acetal carbon GA/PVA
(IV)	2	95.45	hemi-acetal carbon
	3	70.92	α-carbons of crosslinked PVA
	4	64.97	α-carbons of PVA with unreacted -OH
	5	45.27	β-carbons of PVA with unreacted -OH
	6	38.80	α-carbons of crosslinked GA or β-carbons of crosslinked PVA
	7	20.80	β-carbons of crosslinked GA

¹³C CP/MAS NMR results

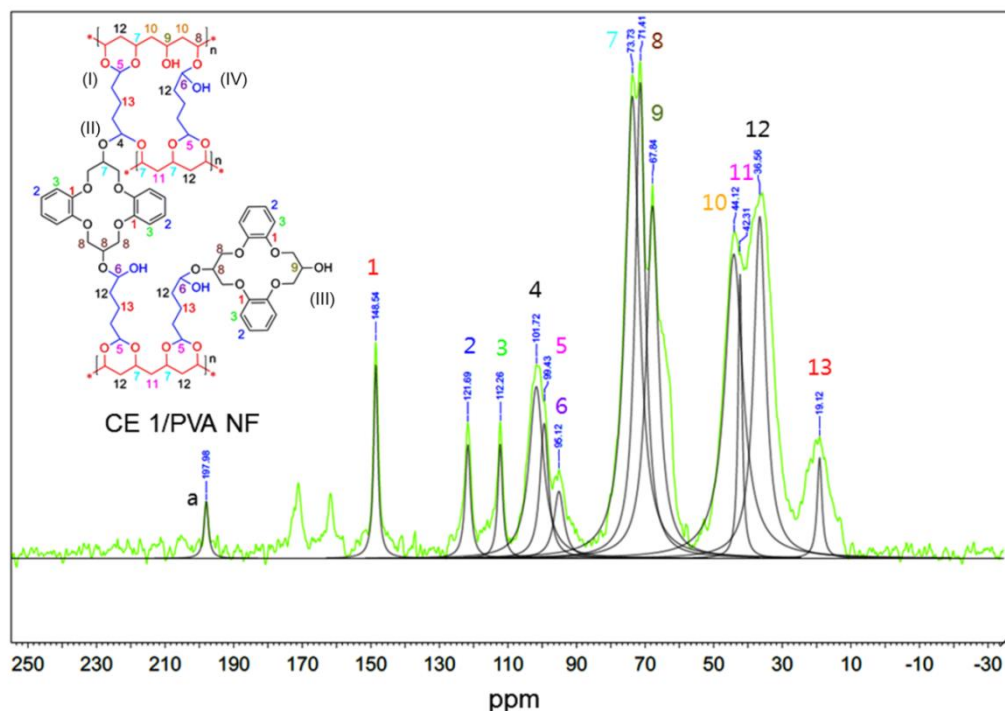


Figure S17. ¹³C CP/MAS NMR of CE 1/PVA MF.

Table S7. Chemical shifts from ¹³C CP/MAS NMR and peak assignments for CE 1/PVA MF.

Crosslink Type	Peak Number	Chemical Shift (δ, ppm)	Assignments
	1	148.54	benzyl carbon bearing O in the CEs
	2	121.69	benzyl carbon (C=C)
	3	112.26	benzyl carbon (C=C)
(II)	4	101.72	acetal carbon CE/GA/PVA linkage
(I)	5	99.43	acetal carbon GA/PVA linkage
(IV)	6	95.12	hemi-acetal carbons between CE/GA or PVA/GA
	7	73.73	α-carbons CE or PVA with O linked to acetal carbon
	8	71.41	carbons bearing O in CE with possible overlaps with: α-carbons of PVA with O linked to hemi-acetal carbon, α,β-carbons in CE with O linked to hemi-acetal carbon
(III)	9	67.84	α-carbons of PVA or CE with unreacted -OH
	10	44.12	β-carbons of PVA with unreacted -OH
	11	42.31	β-carbons of crosslinked PVA
	12	36.56	α-carbons of crosslinked GA or β-carbons of crosslinked PVA
	13	19.12	β-carbons of crosslinked GA
	a	197.98	end carbon of residual aldehyde group

¹³C CP/MAS NMR results

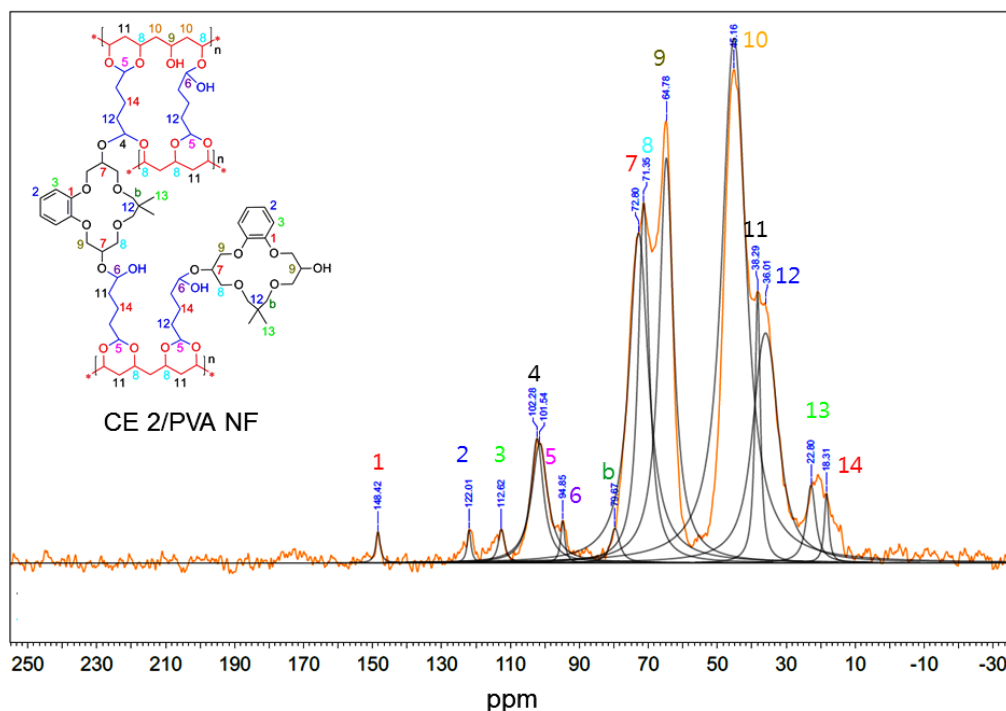


Figure S18. ¹³C CP/MAS NMR of CE 2/PVA MF.

Table S8. Chemical shifts from ¹³C CP/MAS NMR and peak assignments for CE 2/PVA MF.

Crosslink Type	Peak Number	Chemical Shift (δ, ppm)	Assignments
	1	148.42	benzyl carbon bearing ethereal O in the CEs
	2	122.01	benzyl carbon (C=C)
	3	112.62	benzyl carbon (C=C)
(II)	4	102.28	acetal carbon CE/GA/PVA linkage
(I)	5	101.70	acetal carbon GA/PVA linkage
(IV)	6	94.85	hemi-acetal carbons between CE/GA or PVA/GA
	b	79.67	carbons bearing O at the bulky sub-unit of CE ring
	7	72.80	α-carbons of CE with O linked to acetal or hemi-acetal carbon
	8	71.35	α-carbons of PVA O linked to acetal or hemi-acetal carbon with possible overlap with: carbons bearing O at the bulky sub-unit of CE ring
(III)	9	64.78	α-carbons of PVA or CE with unreacted -OH with possible overlap with: carbons bearing O at the benzo-side of CE ring
	10	45.16	β-carbons of PVA with unreacted -OH
	11	38.29	β-carbons of crosslinked PVA with possible overlap with: α-carbons of crosslinked GA (hemi-acetal carbon)
	12	36.01	tertiary carbon in the bulky sub-unit of CE ring with possible overlap with: α-carbons of crosslinked GA (acetal carbon)
	13	20.82	methyl carbons in the bulky sub-unit of CE ring
	14	18.31	β-carbons of crosslinked GA

¹³C CP/MAS NMR results

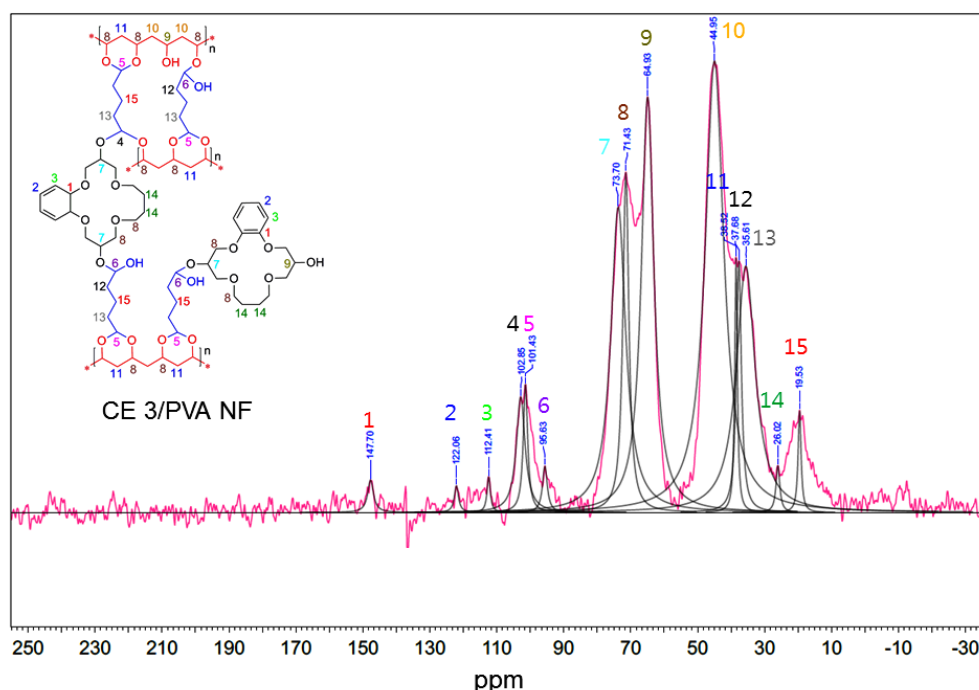


Figure S19. ¹³C CP/MAS NMR of CE 3/PVA MF.

Table S9. Chemical shifts from ¹³C CP/MAS NMR and peak assignments for CE 3/PVA MF.

Crosslink Type	Peak Number	Chemical Shift (δ, ppm)	Assignments
	1	147.70	benzyl carbon bearing ethereal O in the CEs
	2	122.06	benzyl carbon (C=C)
	3	112.41	benzyl carbon (C=C)
(II)	4	102.85	acetal carbon CE/GA/PVA linkage
(I)	5	101.43	acetal carbon GA/PVA linkage
(IV)	6	95.63	hemi-acetal carbons between CE/GA or PVA/GA
	7	73.70	α-carbons of CE with O linked to acetal or hemi-acetal carbon
	8	71.43	carbons bearing O at the butyl sub-unit of CE ring with possible overlaps with: carbons bearing O at the benzo-side of CE ring, α-carbons of PVA with O linked to acetal or hemi-acetal carbon
(III)	9	64.93	α-carbons of PVA or CE with unreacted -OH
	10	44.95	β-carbons of PVA with unreacted -OH
	11	38.52	β-carbons of crosslinked PVA
	12	37.68	α-carbons of crosslinked GA (hemi-acetal carbon)
	13	35.61	α-carbons of crosslinked GA (acetal carbon)
	14	26.02	CH ₂ -CH ₂ carbons at the butyl sub-unit of CE ring
	15	19.53	β-carbons of crosslinked GA

Broad bands at 70 ppm region

Chemical shift predictions (Figure S20) were performed as an attempt to decouple the α,β -carbon resonances in crosslinked PVA and in CEs. In the figure, green bars indicate downfield shifts: lower-end values indicate C peaks of pure CEs in free states [uncrosslinked] and PVA crosslinked in pure form [with GA only]; upper-end values indicate shifted C peaks when CE and PVA were crosslinked together with GA [CE-GA-PVA]. Green arrows indicate chemical shifts of C peaks in CE/PVA samples. Red bars indicate upfield shifts: upper-end values indicate C peaks of CEs in free states [uncrosslinked] and PVA crosslinked in pure form [with GA only]; lower-end values indicate shifted C peaks when CE and PVA were crosslinked together with GA [CE-GA-PVA]. Red arrows indicate chemical shifts of C peaks in CE/PVA samples.

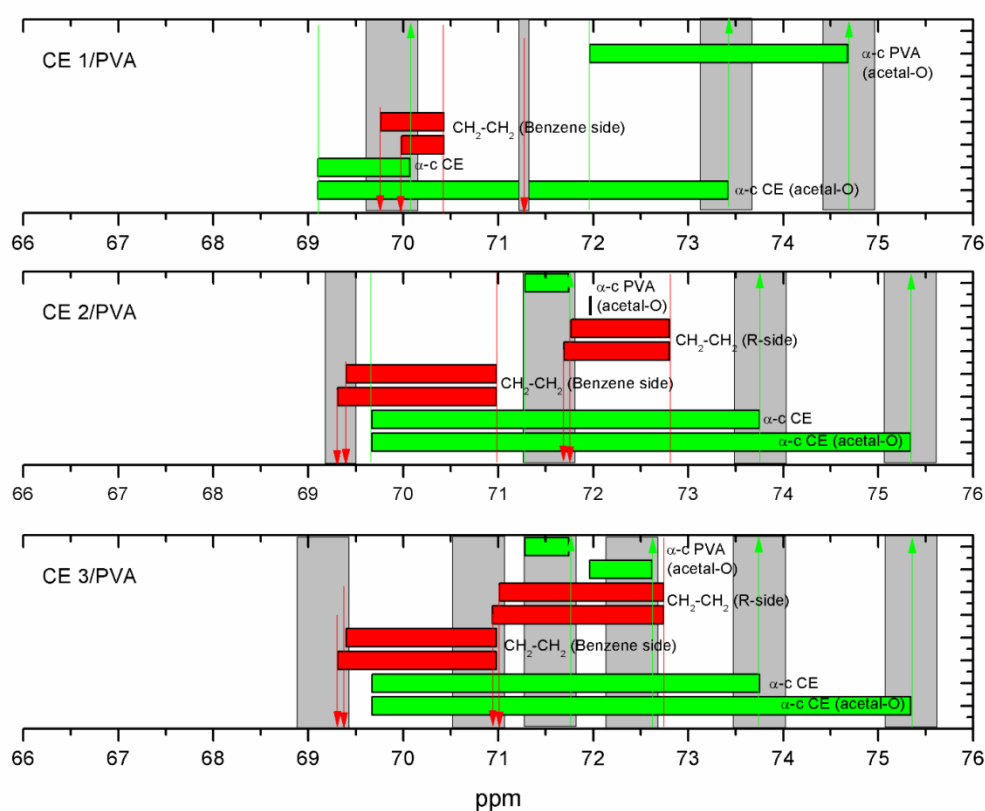


Figure S20. Chemical shift predications of $\text{CH}_2\text{-CH}_2$ in CE rings and $\alpha\text{-C}$ s in crosslinked PVA and CEs using MestRenova 11.0.2.

Simulations (Figure S20) reveal the differences in the chemical shifts of α -carbons of crosslinked pure PVA of the CE/PVA samples. From the three samples, the resonance of the α -carbons in PVA with acetal-linked oxygens was most unique in CE 1/PVA as it exhibited the greatest shift downfield relative to pure PVA ($\sim +4.5$ ppm). Its signal overlapped that of the α -carbons of CEs with acetal-linked oxygens (CE/GA link), which was distinct and remarkably visible at (7). Meanwhile, signals for $\text{CH}_2\text{-CH}_2$ carbons in CE 1 which might have overlapped with the α -carbons of PVA and CE 1 with hemi-acetal linked oxygens, are located upfield (8). In CE 2/PVA and CE 3/PVA, the shifts in signals of α -carbons of

crosslinked PVA were not as remarkable as that in CE 1/PVA. Their signals overlapped with the CH₂-CH₂ carbons of the CE 2 or CE 3 rings and with the α -carbons of PVA with acetal and hemi-acetal linked oxygens (8). Thus, the peak shouldering downfield (7) can be distinctly assigned to the α -carbon of CE 2 or CE 3 components with hemi-acetal and acetal-linked oxygens (CE/GA linkages). These results provide evidence to the successful formation of CE-GA-PVA linkages in the MF samples.

Morphology of uncrosslinked electrospun MFs

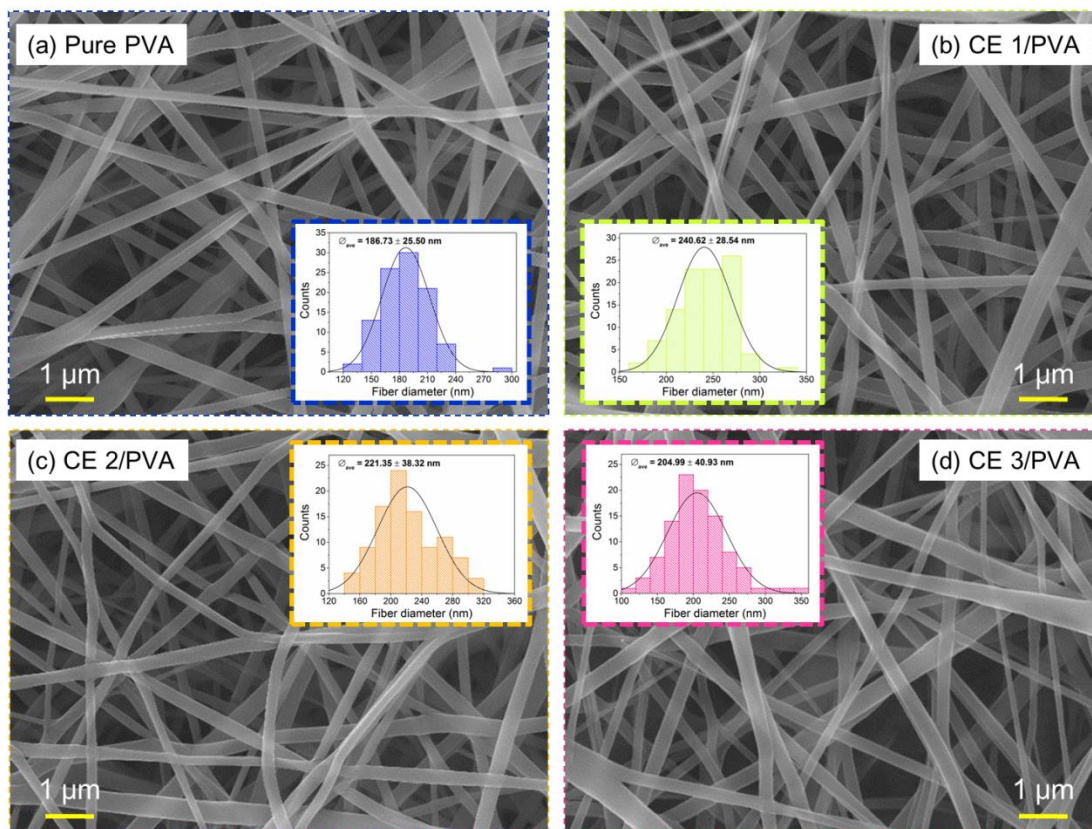


Figure S21. FE-SEM images of MFs before aerosol crosslinking (a) pure PVA and CE/PVA containing: (b) CE 1, (c) CE 2, and (d) CE 3. (Insets: average fiber diameter ($\bar{\phi}_{ave}$) from histograms).

FE-SEM images of uncrosslinked MFs (Figure S21) reveal beadless, smooth, and well-structured fibers. In general, fiber dimensions are affected by the dope solution properties, electrospinning parameters and ambient conditions.¹⁶ Since all MFs were fabricated under the same electrospinning and ambient conditions, the variations in fiber diameters ($\bar{\phi}_{ave}$) must be caused by differences in dope properties which is dependent on the type of melted CEs.¹⁶ The most viscous dope (CE 1/PVA) produced relatively larger fibers (Inset Figure S21b) than the least viscous solution (PVA) (Inset Figure S21a). But it is worthy to mention that a $\Delta\bar{\phi}_{ave} \cong 60$ nm difference between freshly electrospun CE 1/PVA and pure PVA is minor.

Surface analysis and mechanical test results of MF samples

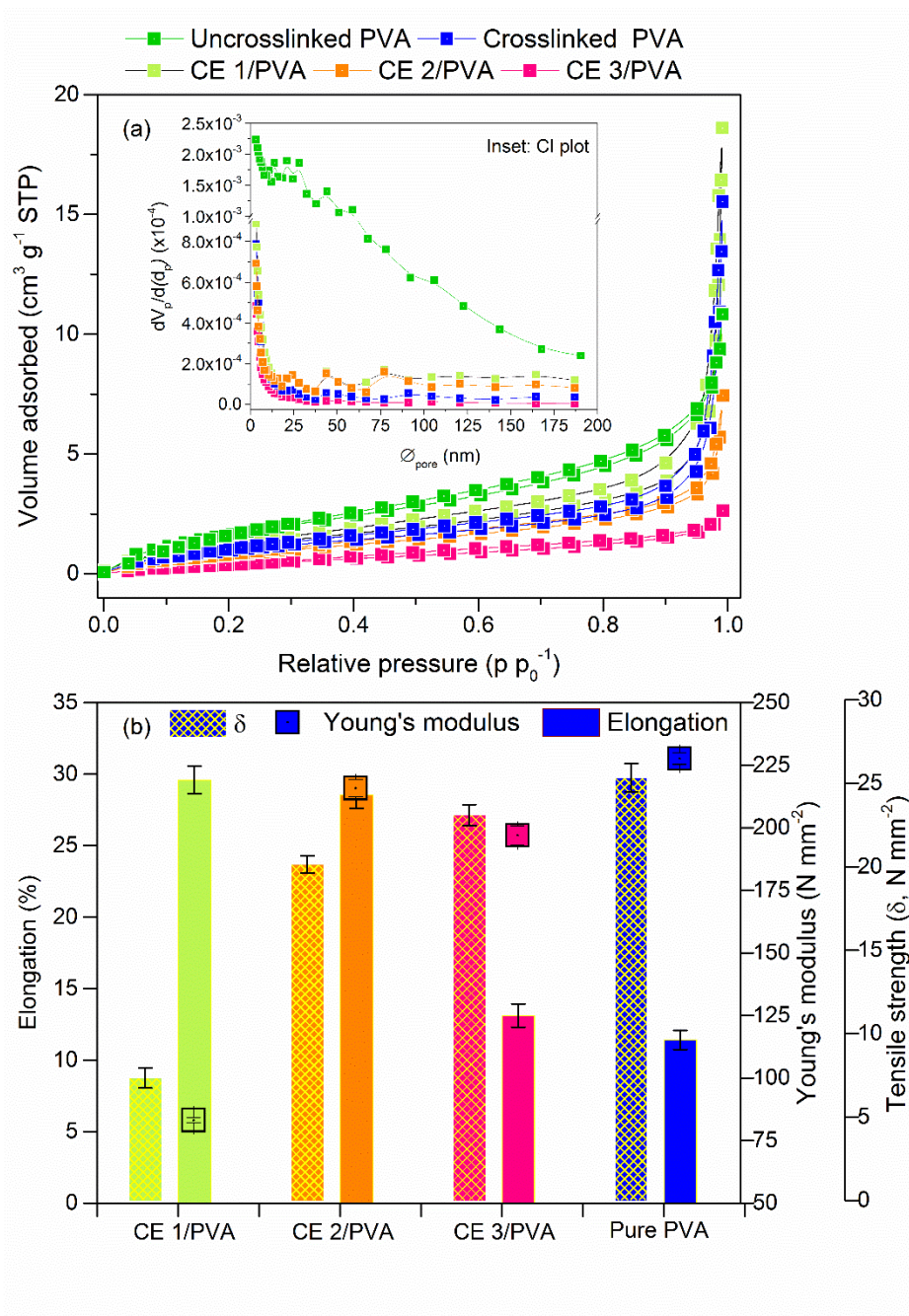


Figure S22. Surface and mechanical properties of MF samples. (a) N₂ adsorption-desorption isotherms (Inset: pore size distribution); (b) Tensile strength, % elongation and Young's modulus.

Pore size distribution (PSD) curves reveal the effect of GA crosslinking in the MFs. Uncrosslinked PVA had the most porous fibers as indicated by the significant presence of macro- ($\varnothing_{\text{pore}} > 50 \text{ nm}$) and/or mesopores ($2 \text{ nm} < \varnothing_{\text{pore}} < 50 \text{ nm}$) (Inset Figure S22a) in contrast to the crosslinked MFs. Among the samples, crosslinked PVA and CE 3/PVA had almost flat PSD curves. The same samples have the lowest v_{pore} values and relatively higher true densities (ρ_{true} , Table 1). These results suggest that pure PVA and CE 3/PVA have the highest fiber packing densities due to intensive GA crosslinking. Meanwhile, internal pores were slightly noticeable in CE 1/PVA and CE 2/PVA MFs as revealed by their PSD curves (Inset Figure S22a). These samples also had relatively higher v_{pore} and lower ρ_{true} (Table 1). These results imply that GA crosslinking is less intense in CE 1/PVA and CE 2/PVA.

Mechanical tests reveal the differences in the durability of the MFs (Figure S22b). CE 1/PVA and CE 2/PVA were easier to deform (% elongation) than CE 3/PVA and pure PVA, which can be attributed to the higher fiber packing density of the latter two samples. Meanwhile, larger fibers mean lower number of fiber-to-fiber contacts. Hence, CE 1/PVA which had the largest \varnothing_{ave} exhibited the lowest δ .¹⁷ Having the highest % elongation and lowest δ , CE 1/PVA also had the lowest Young's modulus among the MFs. Nonetheless, the mechanical properties of all samples including CE 1/PVA are sufficient for their intended application as adsorbents.

Adsorption properties: Effect of solution pH on Li^+ adsorption

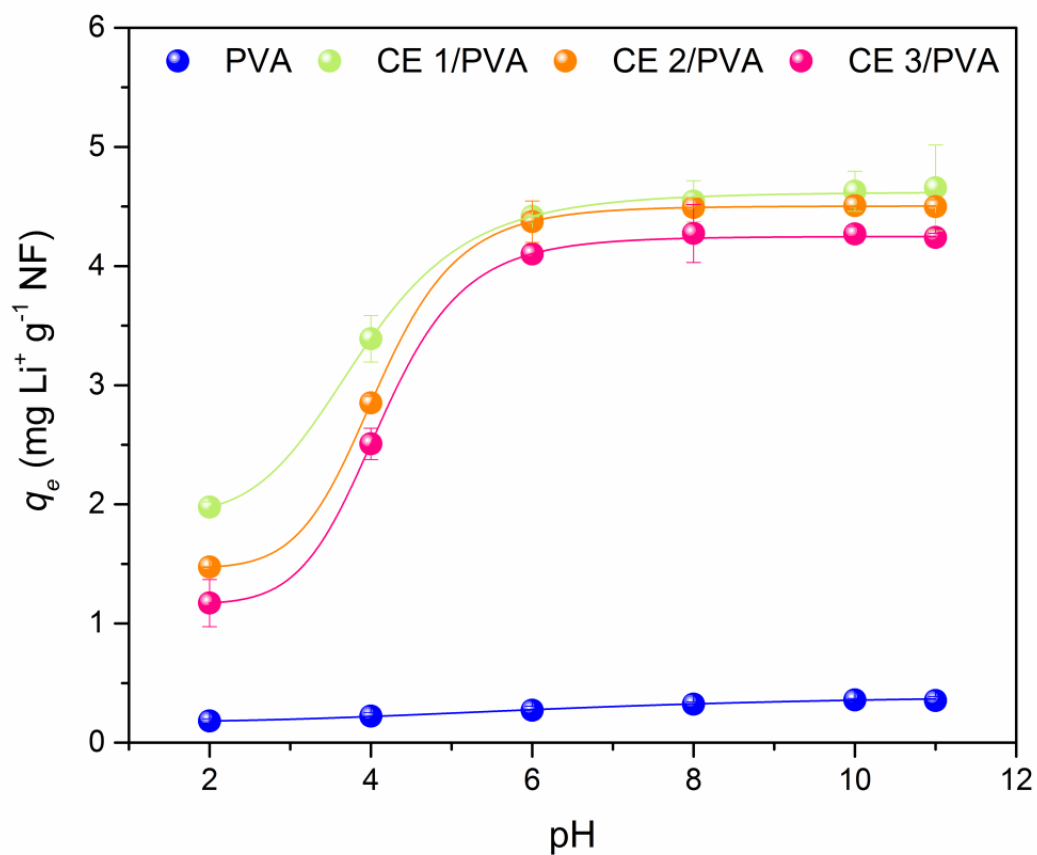


Figure S23. Adsorption results at varied solution pH ($C_0 = 7.35 \text{ mg L}^{-1}$; $m \cong 30 \text{ mg}$; $V = 50 \text{ mL}$; $T = 30^\circ\text{C}$).

Adsorption properties: Non-linear Li^+ adsorption kinetic models

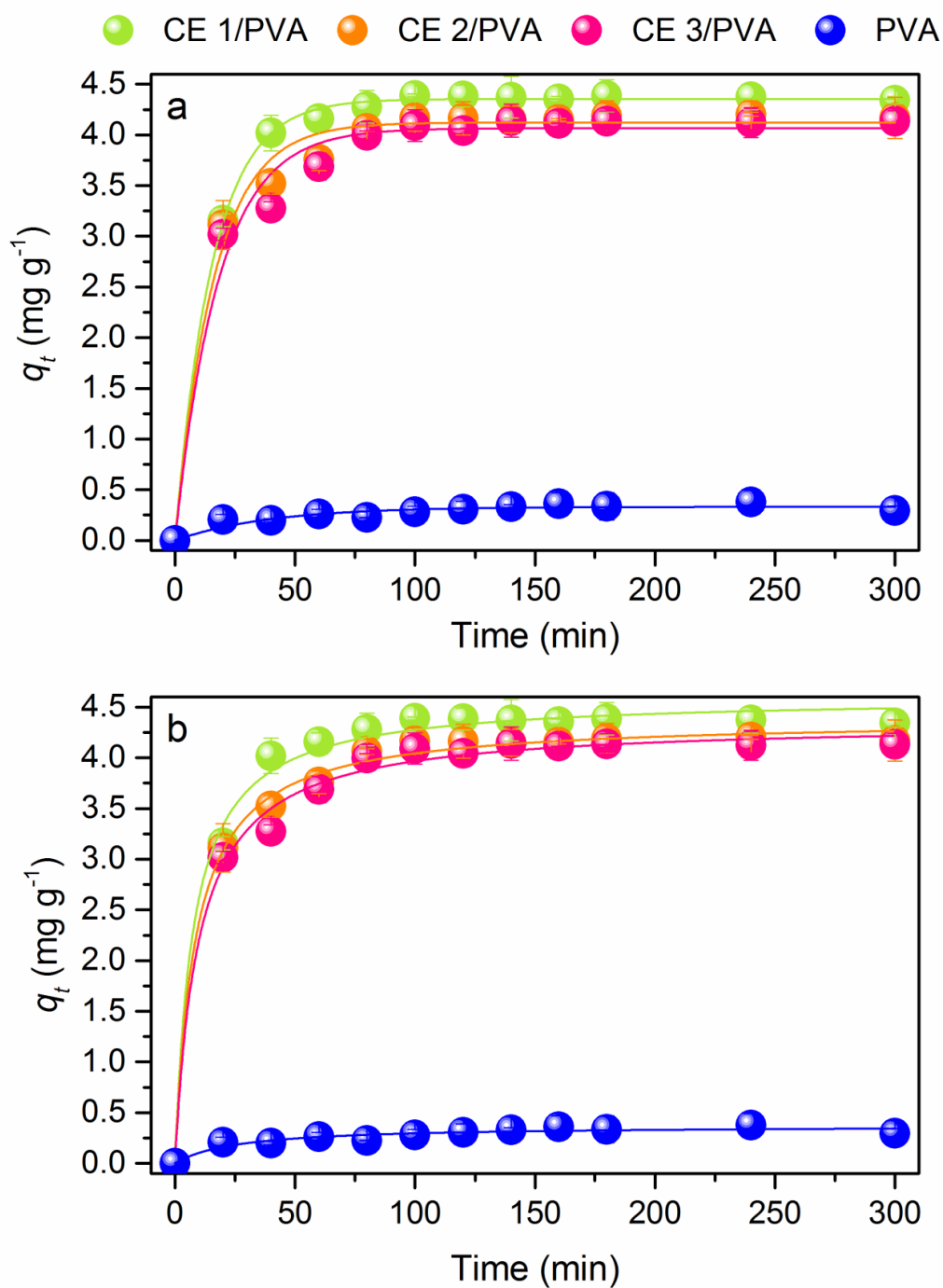


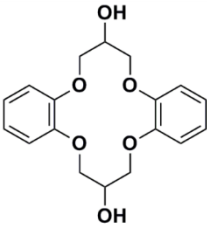
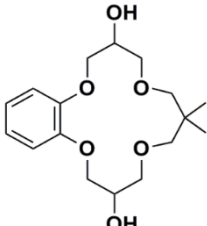
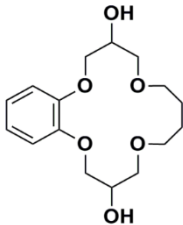
Figure S24. Kinetic rate models for Li^+ adsorption in CE/PVA and pure PVA MFs: (a) pseudo-first and (b) pseudo-second order. ($C_0 = 7.35 \text{ mg L}^{-1}$; $m \cong 30 \text{ mg}$; $V = 50 \text{ mL}$; $T = 30^\circ\text{C}$; $\text{pH} = 8.1$).

Table S10. Li⁺ adsorption performance of inorganic LIS reported in literature.

LIS	Support	Loading content	Delithiation Efficiency	C_o (mg L ⁻¹)	q_e (mg g ⁻¹)	Stabilization time (h)	Reference
λ -MnO ₂	None – powder type	100.00%	-	0.15	0.72	3000 <u>Low kinetics</u>	18
H _{1.39} Li _{0.01} Mn _{1.65} O ₄	None – powder type	100.00%	-	0.17	8.00	5 <i>Moderate kinetics</i>	19
H _{1.6} Mn _{1.6} O ₄	None – powder type	100.00%	99.00%	0.17	40.90	48	20
H _{1.6} Mn _{1.6} O ₄	None – powder type	100.00%	99.00%	5.00	37.00	-	21
H _{1.6} Mn _{1.6} O ₄	None – powder type	100.00%	98.00%	68.85	3.62	-	22
HMn ₂ O ₄	None – powder type	100.00%	40.00% <u>Low efficiency</u>	6.94	10.41	12 <i>Moderate kinetics</i>	23
H ₂ TiO ₃	None – powder type	100.00%	96.62%	15.40	7.64	24 <u>Low kinetics</u>	24
H _{1.33} Mn _{1.67} O ₄	chitosan	80.60%	93.00%	30.00	10.20	168 <u>Low kinetics</u>	25
H _{1.33} Mn _{1.67} O ₄	polyvinyl chloride	80.00%	90.00%	0.17	10.60	360 <u>Low kinetics</u>	26
H _{1.6} Mn _{1.6} O ₄	polyvinyl chloride	15.00%	-	54.20	5.02	-	27
H _{1.6} Mn _{1.6} O ₄	poly(acrylo nitrile)	37.50%	88.70%	15.34	7.43	12 <i>Moderate kinetics</i>	28
H _{1.6} Mn _{1.6} O ₄	polyvinyl alcohol	71.42%	-	11.68	6.82	-	10
HMn ₂ O ₄	pitch	25.00%	93.00%	237.00	1.50	-	29
HMn ₂ O ₄	agar	98.00%	-	0.17	3.40	-	30
HMn ₂ O ₄	magnetite	50.00%	-	0.70	1.20	-	31
H ₄ Mn ₅ O ₁₂	polyvinyl chloride	80.00%	-	222.08	12.44	72 <u>Low kinetics</u>	32
H ₂ TiO ₃	polyvinyl alcohol	72.00%	97.00%	15.00	12.84	12 <i>Moderate kinetics</i>	33

Adsorption properties: Theoretical adsorption capacities of CEs (q_{theo})

Table S11. Theoretical adsorption capacities of pure CEs.

Type	Structure	MW (g mol ⁻¹)	q_{theo} (mg Li ⁺ g ⁻¹ CE)	
			1 mole of CE with mole of Li ⁺ (1:1)	2 moles of CEs with 1 mole of Li ⁺ (2:1)
CE 1		332.34	20.89	10.44
CE 2		326.38	21.27	10.63
CE 3		312.35	22.22	11.11
Li ⁺		6.941		

Adsorption properties: Non-linear Li^+ adsorption isotherm models

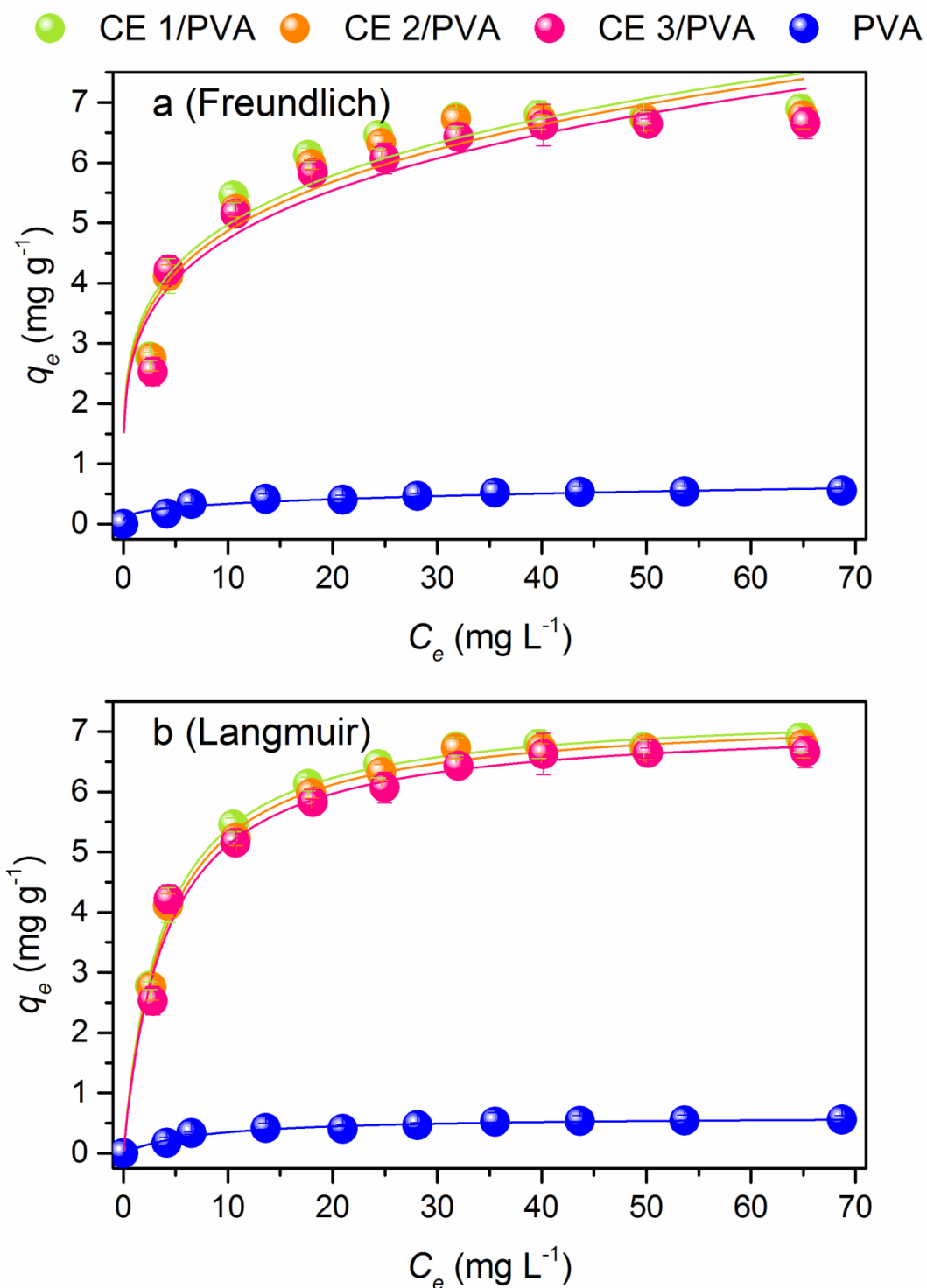


Figure S25. Isotherm models for Li^+ adsorption in CE/PVA and pure PVA MFs: (a) Freundlich (b) Langmuir. ($C_0 = 3 - 70 \text{ mg L}^{-1}$; $m \cong 30 \text{ mg}$; $V = 50 \text{ mL}$; $T = 30^\circ\text{C}$; $\text{pH} = 8.0$).

Table S12. Li⁺ adsorption performance of CE-based Li⁺ adsorbents reported in literature.

CE Type	CE Name	Support	Nominal CE loading (mmole g ⁻¹)	Actual CE loading (mmole g ⁻¹)	Fabrication CE loss (%)	q_{theo} (mg g ⁻¹)	q_e (mg g ⁻¹)	Adsorption loss (%)	C_a (mg L ⁻¹)	Stabilization time (min)	Reference
CE 12	CE with pendant vinyl group	Silica gel	0.18	0.18 <u>Low CE loading</u>	-	1.24	0.01	98.83 <u>High adsorption loss</u>	0.14	-	34
CE 12	2-Hydroxymethyl-12-crown-4	SBA-15	0.89	0.87 <u>Moderate CE loading</u>	2.24 Low CE loss	6.00	7.63	+27 % excess <u>Low selectivity</u>	34.70	-	35
CE 12	2-(allyloxy) methyl-12-crown-4	Magnetite	0.61	0.61 <u>Low CE loading</u>	-	4.24	4.03	5.11 Low adsorption loss	3.47	10	36
CE 14	CE with pendant vinyl group	Silica gel	0.17	0.17 <u>Low CE loading</u>	-	1.17	0.05	96.01 <u>High adsorption loss</u>	0.14	-	34
CE 14	Hydroxy-dibenzo-14-crown-4	MWCNT	2.27	1.71 High CE loading	24.57 <u>Moderate CE loss</u>	11.87	5.41	54.39 <u>High adsorption loss</u>	111	-	37
CE 14	Hydroxy-dibenzo-14-crown-4	MWCNT	2.27	1.71 High CE loading	24.57 <u>Moderate CE loss</u>	11.87	2.50	78.93 <u>High adsorption loss</u>	35	-	37
CE 14	Methyl-14-crown-4-OH	Poly(glycidyl methacrylate) PGMA	2.50	0.44 <u>Low CE loading</u>	82.4 <u>High CE loss</u>	3.05	3.05	-	694	-	38
CE 14	2HDB14C4	Glutaraldehyde/polyvinyl alcohol (GA/PVA)	1.00	1.001 High CE loading	0.23 Negligible CE loss	6.96	6.90	0.93 Low adsorption loss	70	120	This study
CE 14	2HDB14C4		-	-	-	6.53	6.51	0.35 Low adsorption loss	70	120	This study
CE 15	Benzo-15-Crown-5	Mesoporous silica	2.3x10 ⁻³	2.94x10 ⁻⁵ <u>Low CE loading</u>	98.73 <u>High CE loss</u>	0.20	0.18	11.39 Low adsorption loss	139	480	39
CE 15	Diamino-dibenzo-15-crown-5		1.77	1.77 High CE loading	-	12.25	3.43	72.00 <u>High adsorption loss</u>	6940	-	40
CE 15	2HB2M15C4	Glutaraldehyde/polyvinyl alcohol (GA/PVA)	1.02	1.016 High CE loading	0.54 Negligible CE loss	7.08	6.78	4.30 Low adsorption loss	70	120	This study
CE 15	2HB2M15C4		-	-	-	6.61	6.40	3.17 Low adsorption loss	70	120	This study
CE 16	Dibenzo-16-crown 5	Condensation polymerization (formaldehyde/formic acid)	2.39	1.75 High CE loading	26.77 <u>Moderate CE loss</u>	12.15	2.29	81.14 <u>High adsorption loss</u>	694	-	41
CE 16	Dibenzo-16-crown 5	Condensation polymerization (formaldehyde/formic acid)	2.17	1.46 High CE loading	32.76 <u>Moderate CE loss</u>	10.13	1.60	84.25 <u>High adsorption loss</u>	694	-	41
CE 16	2HB16C4	Glutaraldehyde/polyvinyl alcohol (GA/PVA)	1.07	1.066 High CE loading	0.12 Negligible CE loss	7.41	6.66	10.08 Low adsorption loss	70	120	This study
CE 16	2HB16C4		-	-	-	6.96	6.27	9.75 Low adsorption loss	70	120	This study
CE 18	Dibenzo-18-crown-6	Polyacrylo-nitrile	0.25	0.25 <u>Low CE loading</u>	-	1.75	1.11	36.63 <u>High adsorption loss</u>	69.40	480	7
CE 18	Diamino-dibenzo-18-crown-6	Biphenyl Tetracarboxylic Acid	1.46	1.46 High CE loading	-	10.14	3.95	60.99 <u>High adsorption loss</u>	6940	-	40
CE 18	Diaza-18-crown-6	Dianhydride (BPDA)	1.80	1.80 High CE loading	-	12.47	2.99	75.99 <u>High adsorption loss</u>	6940	-	40

Legends:

⁺ Theoretical q_e = actual CE loading (mmol g⁻¹) × 6.941 mg mmol⁻¹

⁺ Experimental q_e as mg Li⁺ g⁻¹ MF

For selected entries (CE adsorption contributions on q_e of CE/PVA MFs):

[#] Theoretical $q_e = q_{theo} \cdot f'_{CE} \rightarrow (q_{theo} \text{ values are listed in Table S10 for 1:1 complexation})$

[#] Experimental $q_e = q_{CE} \cdot f'_{CE} \rightarrow \text{CE adsorption contribution defined in Eq. 7 of main article}$

Stabilization time – onset of equilibrium time

Density Functional Theory calculations

Table S13. Average opposite O distances, [O-O]_{ave} before and after complexation of CEs with Mⁿ⁺.

CE	Free CE [O-O] _{ave}	CE-Li ⁺ [O-O] _{ave}	CE-Na ⁺ [O-O] _{ave}	CE-K ⁺ [O-O] _{ave}	CE-Mg ²⁺ [O-O] _{ave}	CE-Ca ²⁺ [O-O] _{ave}	Free CE cavity size
CE 1	3.87±0.00	3.83±0.00	3.87±0.01	3.79±0.00	3.85±0.00	3.91±0.00	1.23±0.00
CE 2	4.16±0.01	3.98±0.16	4.16±0.06	4.08±0.14	4.01±0.13	4.10±0.00	1.52±0.01
CE 3	4.43±0.02	4.16±0.52	4.45±0.13	4.44±0.08	4.08±0.33	4.39±0.11	1.79±0.02
Estimated cavity size after 1:1 CE-Mⁿ⁺ complexation^a							
CE	CE-Li ⁺	CE-Na ⁺	CE-K ⁺	CE-Mg ²⁺	CE-Ca ²⁺	Average	
CE 1	1.19±0.00	1.23±0.00	1.15±0.00	1.21±0.00	1.27±0.00	1.21±0.04	
CE 2	1.34±0.16	1.52±0.06	1.44±0.14	1.52±0.01	1.46±0.00	1.45±0.07	
CE 3	1.52±0.52	1.81±0.13	1.80±0.08	1.56±0.16	1.79±0.06	1.70±0.14	

^a Estimated cavity size by the distance of two opposite ethereal O atoms [O-O]_{ave} of the free or CE-Mⁿ⁺ complex subtracted by the effective ionic radius of ethereal O (1.32 Å). Cavity size = [O-O]_{ave} – (1.32x2), for the two ethereal O atoms.⁴²

A reduction or expansion of the CE ring suggests conformational change in its structure to accommodate the Mⁿ⁺.¹⁹ In general, all CEs had reduced CE cavities after Mⁿ⁺ complexation except for Ca²⁺ which caused CE 1 to expand, same as Na⁺ and K⁺ in CE 3. Meanwhile, all Mⁿ⁺ except for Na⁺ reduced the cavity size of CE 2. The least changes in CE cavities were observed in CE 1, which confirms that the dibenzo units rigidified its ring most effectively. On the other hand, the bulky sub-unit on one side of CE 2 resulted in its moderate conformational change while the flexible butyl chain in CE 3 permitted the greatest movement of its ring.⁴²

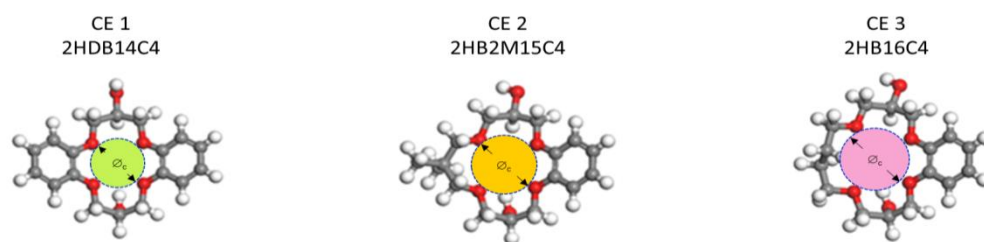
Table S14. O-Mⁿ⁺ distances (Å) of CE-Mⁿ⁺ complexes calculated using DFT PBE-PAW level of theory.

CE	O-Li ⁺		O-Na ⁺		O-K ⁺		O-Mg ²⁺		O-Ca ²⁺	
	Bulky side	Rigid side	Bulky side	Rigid side	Bulky side	Rigid side	Bulky side	Rigid side	Bulky side	Rigid side
CE 1	1.93±0.01	1.93±0.01	2.29±0.01	2.29±0.01	2.71±0.01	2.71±0.01	2.02±0.01	2.02±0.01	2.27±0.00	2.27±0.00
CE 2	2.00±0.01	2.04±0.04	2.25±0.00	2.24±0.01	2.69±0.01	2.67±0.01	2.02±0.03	2.07±0.02	2.26±0.01	2.27±0.00
CE 3	2.14±0.07	2.06±0.00	2.27±0.00	2.26±0.00	2.71±0.01	2.68±0.01	2.05±0.03	2.09±0.01	2.34±0.01	2.34±0.01

Bulky side O-Mⁿ⁺ distances refers to the distance between Mⁿ⁺ and ethereal O atoms near the bulky subunit structure while the rigid side O-Mⁿ⁺ distance refers to the ethereal O atoms near the aromatic group.

The O-M⁺ distances varied according to the Mⁿ⁺ which generally increased with the ionic size. The trend was easily seen in CE 1 which has a symmetric ring, it also showed the same O-Mⁿ⁺ distances on its both sides for each type of Mⁿ⁺. Meanwhile CE 2 was able to block larger Mⁿ⁺. The higher O-M⁺ distances at its bulky side suggest repulsion of Mⁿ⁺ towards the benzyl group, which reduce the stability of the complexes particularly those of Na⁺ and K⁺. In contrast, smaller Mⁿ⁺ like Li⁺ and Mg²⁺ were closer to the bulky side suggesting more stable complexes. Meanwhile, the butyl side of CE 3 exhibited better accommodation for Mg²⁺ than Li⁺. It also showed low blockage response to larger Mⁿ⁺ suggesting its relatively lower ability to discriminate ions according to their size than CE 1 and CE 2.

Optimized Structures of CE diols



Optimized Structures of 1:1 CE-Mⁿ⁺ complex

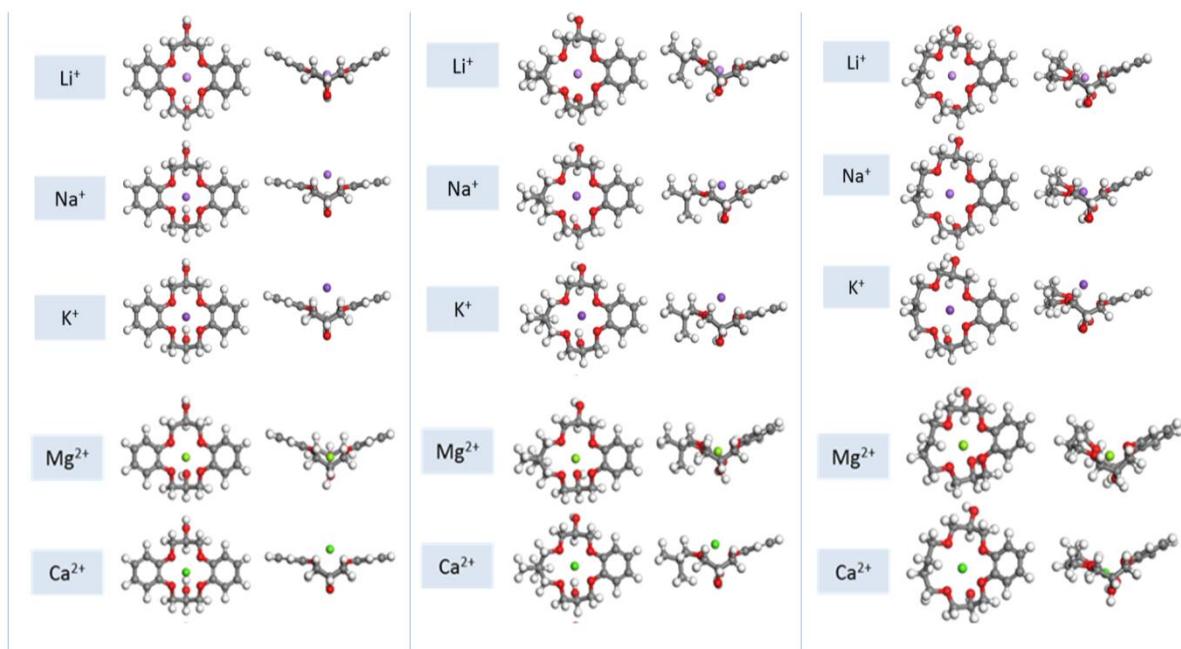


Figure S26. Lowest energy conformation of free and 1:1 CE-Mⁿ⁺ complexed optimized using DFT PBE-PAW level of theory.

Exothermicity of exchange of reactions

$$\Delta H_n = \Delta H[M^{n+}(CE)] + \Delta H[Li^+(H_2O)_n] - \Delta H[Li^+(CE)] - \Delta H[M^{n+}(H_2O)_n]$$

Table S15. Binding enthalpies (ΔH) for the M^{n+} (CE) complexes.

CE	ΔH_{Li} (kcal mol ⁻¹)	ΔH_{Na} (kcal mol ⁻¹)	ΔH_K (kcal mol ⁻¹)	ΔH_{Mg} (kcal mol ⁻¹)	ΔH_{Ca} (kcal mol ⁻¹)
CE 1	-80.54	-46.29	-27.18	-247.17	-150.44
CE 2	-91.16	-54.09	-32.94	-263.35	-162.13
CE 3	-81.90	-59.23	-37.43	-262.93	-192.41

Table S16. Binding enthalpies (ΔH) for the $M^{n+}(H_2O)_n$ where $n=6$.⁴³

Metal Ion	ΔH (kcal mol ⁻¹)
Li ⁺	-122.9
Na ⁺	-95.6
K ⁺	-79.9
Cs ⁺	-64.0
Mg ²⁺	-316.5
Ca ²⁺	-245.3
Sr ²⁺	-213.6

Table S17. ΔH_n values of M^{n+} relative to Li^+ ($\Delta H_n = 0$ kcal mol⁻¹).

CE	$\Delta H_n (Li^+ - Li^+)$ kcal mol ⁻¹	$\Delta H_n (Li^+ - Na^+)$ kcal mol ⁻¹	$\Delta H_n (Li^+ - K^+)$ kcal mol ⁻¹	$\Delta H_n (Li^+ - Mg^{2+})$ kcal mol ⁻¹	$\Delta H_n (Li^+ - Ca^{2+})$ kcal mol ⁻¹
CE 1	0.00	6.95	10.36	37.59	63.12
CE 2	0.00	9.77	15.22	21.41	51.43
CE 3	0.00	-4.63	1.47	21.83	21.15

Recycling experiments

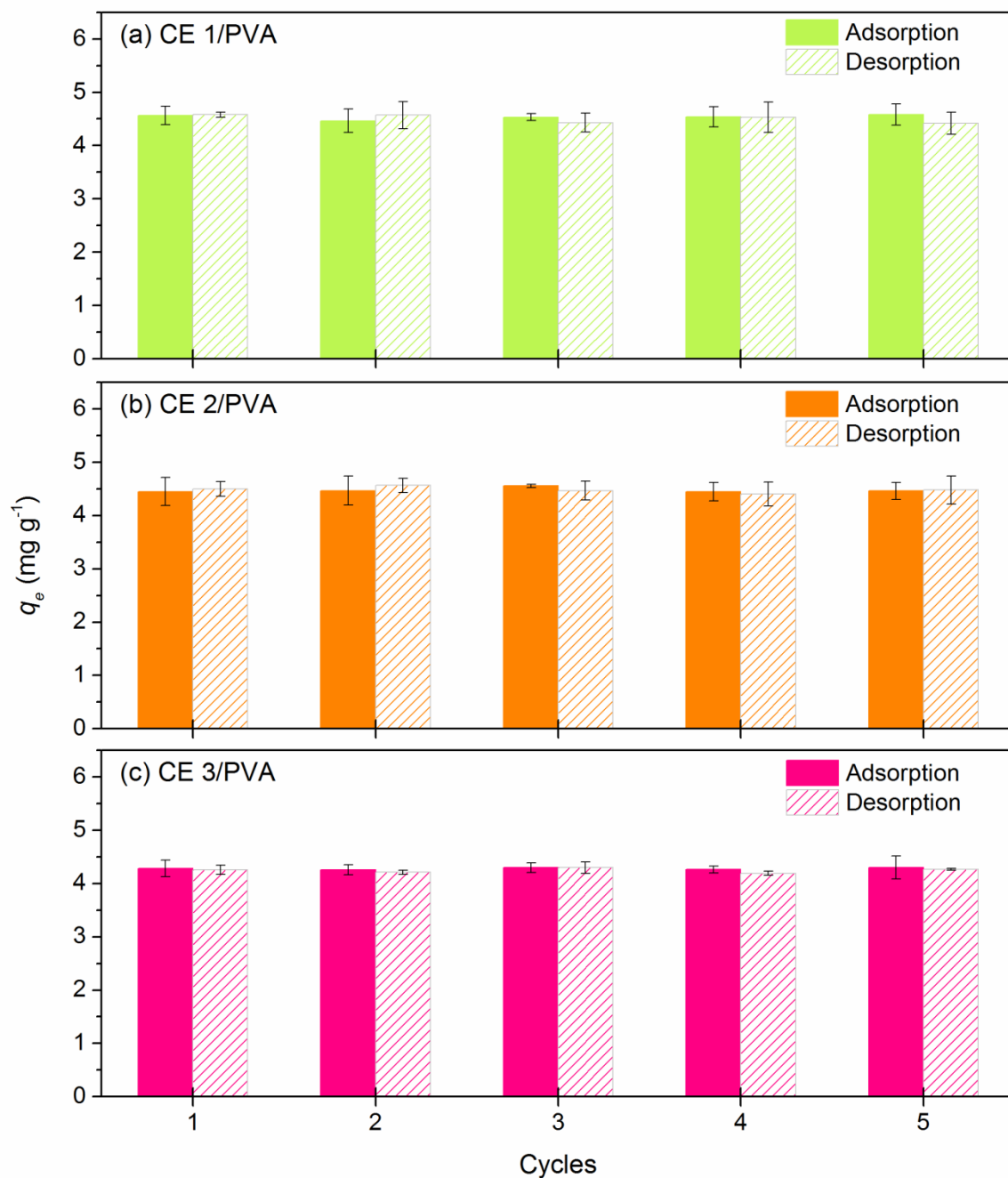


Figure S27. Cycled Li^+ adsorption/desorption runs for regenerability tests of the CE/PVA MFs: (a) CE 1/PVA (b) CE 2/PVA and (c) CE 3/PVA. ($C_0 = 6.7 \text{ mg L}^{-1}$; $m \cong 30 \text{ mg}$; $V = 50 \text{ mL}$; $T = 30^\circ\text{C}$; $\text{pH} = 8.0$).

MF autopsy after five adsorption/desorption cycles

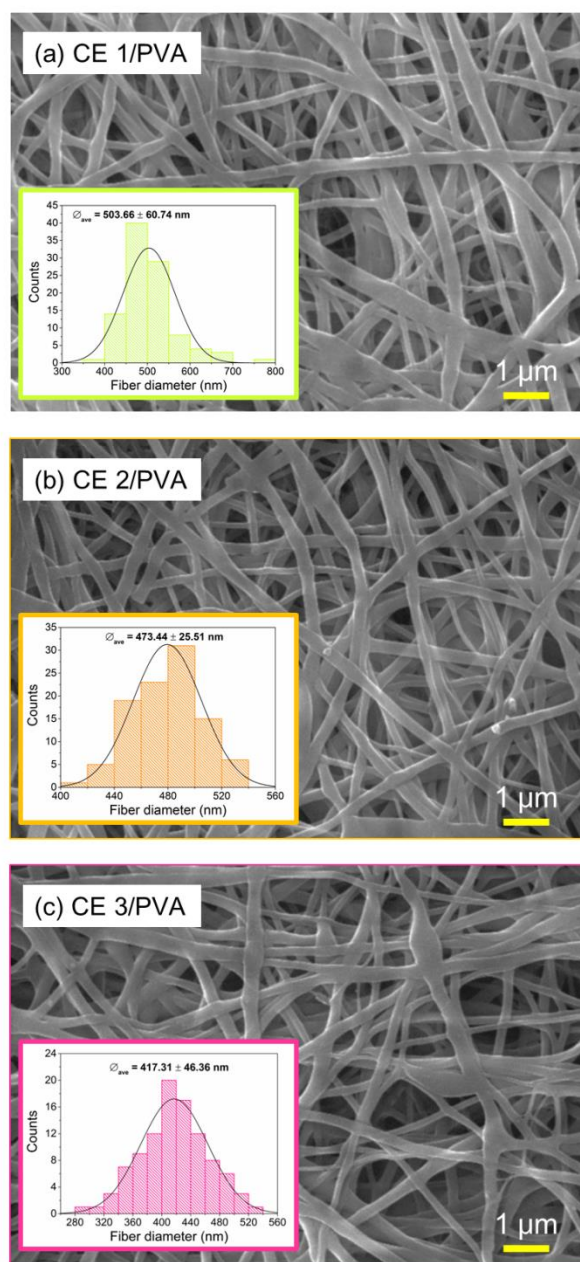


Figure S28. SEM images of used CE/PVA MFs after 5th adsorption/desorption cycle: (a) CE 1/PVA (b) CE 2/PVA and (c) CE 3/PVA.

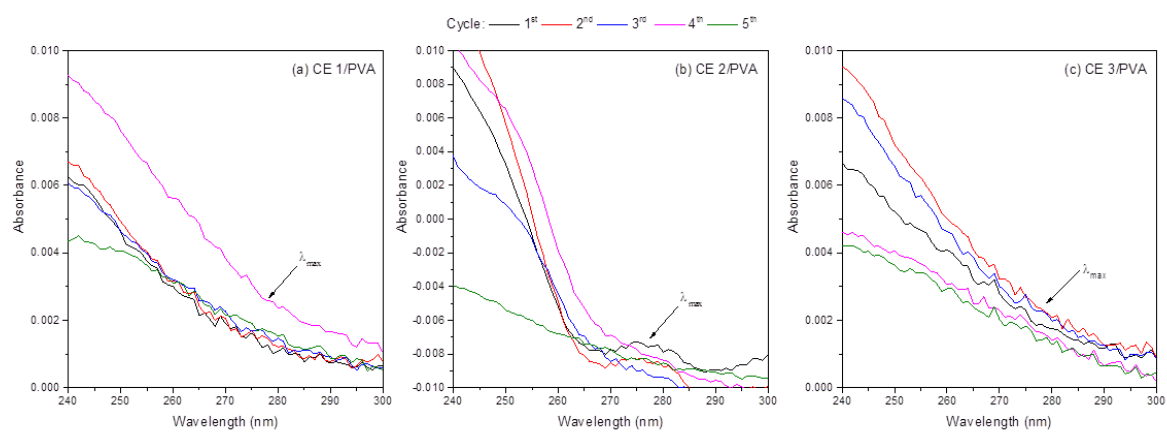


Figure S29. UV-Vis spectra of stripping solutions (0.5 M HCl) used to desorb Li^+ from spent CE/PVA MFs (for eluted CE detection): (a) CE 1/PVA (b) CE 2/PVA and (c) CE 3/PVA.

Nomenclature:

<i>Symbols</i>	<i>Description</i>
\varnothing	– diameter (\AA or mm)
[]	– concentration (mg L^{-1})
Δ	– difference
δ	– tensile strength (N mm^{-2})
δ	– chemical shift (ppm)
ρ	– density (g cm^{-3})
λ	– wavelength in UV-Vis spectrophotometer analysis (nm)
α	– separation factor
a	– area (cm^2)
Abs	– absorbance (AU)
C	– concentration (mg L^{-1})
f	– weight fraction (unitless)
H	– binding enthalpy (kcal mol^{-1})
I	– integrated FTIR peaks (unitless)
k	– rate constant (k_1 : min^{-1} ; k_2 : $\text{g mg}^{-1} \text{min}^{-1}$)
K	– adsorption isotherm constant (K_L : L mg^{-1} ; K_F : mg g^{-1})
K_d	– distribution coefficient (mL g^{-1})
L	– liquid; aqueous solution component (in S/L ratio)
m	– mass (mg)
M	– metal (Li, Na, Mg, K, Ca)
n	– number of measurements or trials
n	– Freundlich adsorption intensity (unitless)
p	– pressure
P	– porosity (%)
q	– adsorption capacity (mg g^{-1})
r^2	– statistical coefficient of determination (unitless)
S	– solid; adsorbent component (in S/L ratio)
S	– swelling ratio (unitless)
t	– time (min or h)
T	– temperature ($^{\circ}\text{C}$)
v	– volume (e.g. v_{pore} , $\text{cm}^3 \text{g}^{-1}$)
V	– volume (mL or L)
w	– weight (mg)
l	– distance (nm)
N	– Avogadro's number

Subscripts

o	– initial at $t = 0$
1	– pristine MF (in Table S2)
2	– unwashed crosslinked MF (in Table S2)
3	– washed and dried cross-linked MF (in Table S2)
ave	– average
<i>Avogadro</i>	– Avogadro's number
<i>bulk</i>	– density measured via dimensional measurement (in ρ_{bulk})

<i>c</i>	–	CE cavity
<i>C</i>	–	carbon
<i>C-CE</i>	–	carbon from CE component
<i>C-PVA</i>	–	carbon from PVA component
<i>CE_loss</i>	–	CE eluted from fiber
<i>e</i>	–	equilibrium
<i>eluent</i>	–	soaking deionized water
<i>inner</i>	–	inner diameter (in $\varnothing_{\text{inner}}$)
<i>F</i>	–	Freundlich adsorption isotherm model
<i>L</i>	–	Langmuir adsorption isotherm model
<i>m</i> or <i>max</i>	–	maximum
<i>n</i>	–	number of surrounding H ₂ O molecules (in Eq. 11).
<i>out</i>	–	outer
<i>P</i>	–	characteristic FTIR peaks
<i>pore</i>	–	pores in MF samples
<i>PVA_loss</i>	–	PVA eluted from fiber
<i>t</i>	–	time (min)
<i>theo</i>	–	theoretical
<i>true</i>	–	density measured via pycnometer (in ρ_{true})
<i>UV-Vis</i>	–	measured by UV-Vis spectrophotometry

Superscripts

<i>n+</i>	–	cation charge number (1,2)
<i>'</i>	–	actual (<i>f'</i> , <i>m'</i>)

Abbreviations

BET	–	Brunauer, Emmett and Teller
CE	–	Crown ether
<i>CF</i>	–	Concentration factor (L g ⁻¹)
CI	–	Cranston-Inkley model
DFT	–	Density functional theory
PBE	–	Perdew-Burke-Ernzerhof
PAW	–	Projector augmented wave
DI	–	Deionized
FESEM	–	Field Emission Scanning Electron Microscope
FTIR	–	Fourier-transform infrared spectroscopy
GA	–	Glutaraldehyde
ICP-MS	–	Inductively coupled plasma mass spectrometry
LIS	–	Lithium ion sieve
MWCNT	–	Multi-walled carbon nanotube
mCE	–	Methylated crown ether
MF	–	Microfiber
PVA	–	Poly(vinyl alcohol)
PSD	–	Pore size distribution
RBF	–	Round bottom flask
SA	–	Surface area (m ² g ⁻¹)

SS	–	Solid-state
CP-MAS	–	Cross-polarization-magic angle spinning
NMR	–	Nuclear magnetic resonance spectroscopy
TOC	–	Total organic carbon
2HDB14 C4	–	6,7,8,15,16,17-hexahydrodibenzo [1,4,8,11] tetraoxacyclotetradecine-7,16-diol (CE 1)
2HB2M1 5C4	–	7,7-dimethyl-3,4,6,7,8,10,11,12-octahydro- 2H benzo [1,4,8,12] tetraoxa-cyclopentadecine-3,11-diol (CE 2)
2HB16C4	–	2,3,4,6,7,8,9,11,12,13-decahydrobenzo[1,4,8,13] tetraoxacyclohexadecine-3,12-diol (CE 3)

References:

1. Zaagsma, J.; Nauta, W.Th. β -Adrenoceptor Studies. 1. In Vitro β -Adrenergic Blocking, Antiarrhythmic, and Local Anaesthetic Activities of a New Series of Aromatic Bis(2-hydroxy-3-isopropylaminopropyl) Ethers. *J. Med. Chem.* **1974**, *17*, 507-513.
2. Olsher, U.; Frolow, F.; Shoham, G.; Luboch, E.; Yu, Z.Y.; Bartsch, R.A. Synthesis and Selectivity of sym-Hydroxydibenzo-14-Crown-4 Ionophores for Protons, Alkali Metal Cations, and Alkaline Earth Cations in Polymeric Membranes. *J. Incl. Phenom. Mol. Recognit. Chem.* **1990**, *9*, 125-135.
3. Nakatsuji, Y.; Tsuji, Y.-I.; Ikeda, I.; Okahara, M. Reactions of Oligoethylene Glycol Diglycidyl Ethers with Hydroxy Compounds. *J. Org. Chem.* **1986**, *51*, 78-81.
4. Destaye, A.G.; Lin, C.-K.; Lee, C.-K. Glutaraldehyde Vapor Cross-linked Nanofibrous PVA Mat with in Situ Formed Silver Nanoparticles. *ACS Appl. Mater. Interfaces* **2013**, *5*, 4745-4752.
5. dos Reis, E.F.; Campos, F.S.; Lage, A.P.; Leite, R.C.; Heneine, L.G.; Vasconcelos, W.L.; Lobato, Z.I.P.; Mansur, H.S. Synthesis and Characterization of Poly (Vinyl Alcohol) Hydrogels and Hybrids for rMPB70 Protein Adsorption. *Mat. Res.* **2006**, *9*, 185-191.
6. Nakanishi, K.; Solomon, K. *Infrared Absorption Spectroscopy*, 2nd ed; Holden-Day: Oakland, California, USA, 1977.
7. Tas, S.; Kaynan, O.; Ozden-Yenigun, E.; Nijmeijer, K. Polyacrylonitrile (PAN)/Crown Ether Composite Nanofibers for the Selective Adsorption of Cations. *RSC Adv.* **2016**, *6*, 3608-3616.
8. Yeom, C.-K.; Lee, K.-H. Pervaporation Separation of Water-Acetic Acid Mixtures through Poly (Vinyl Alcohol) Membranes Crosslinked with Glutaraldehyde. *J. Memb. Sci.* **1996**, *109*, 257-265.
9. Moore, T.T.; Koros, W.J. Gas Sorption in Polymers, Molecular Sieves, and Mixed Matrix Membranes. *J. Appl. Polym. Sci.* **2007**, *104*, 4053-4059.
10. Nisola, G.M.; Limjuco, L.A.; Vivas, E.L.; Lawagon, C.P.; Park, M.J.; Shon, H.K.; Mittal, N.; Nah, I.W.; Kim, H.; Chung, W.-J. Macroporous Flexible Polyvinyl Alcohol Lithium Adsorbent Foam Composite Prepared via Surfactant Blending and Cryo-Desiccation. *Chem. Eng. J.* **2015**, *280*, 536-548.
11. Togrul, M.; Turgut, Y.; Hosgoren, H. Enantioselective Recognition of Ammonium Perchlorate Salts by Optically Active Monoaza-15-crown-5 Ethers. *Chirality* **2004**, *16*, 351-355.
12. Postulkova, H. Chemical modifications of hydrogels from natural polysaccharide. Master's Thesis, Brno University of Technology, Brno, Czech Republic, 2014.

13. An, Y.; Koyama, T.; Hanabusa, K.; Shirai, H. Preparation and Properties of Highly Phosphorylated Poly (Vinyl Alcohol) Hydrogels Chemically Crosslinked by Glutaraldehyde. *Polym.* **1995**, *36*, 2297-2301.
14. Hagiopol, C.; Johnston, J.W. *Chemistry of Modern Papermaking*; CRC Press: Florida, USA, 2011.
15. Buchanan, G.W.; Kirby, R.A.; Charland, J.P. Stereochemistry of Crown Ethers and Their Complexes in the Solid State. ^{13}C CPMAS NMR and X-ray Crystallographic Studies of Configurationally Isomeric Dicyclohexano-14-Crown-4 Ethers, Dibenzo-14-Crown-4 Ether, and Some Lithium Thiocyanate Salts. *J. Am. Chem. Soc.* **1988**, *110*, 2477-2483.
16. Li, Z.; Wang, C. *Electrospinning in One-Dimensional Nanostructures*; Springer: Germany, 2013.
17. Amiraliyan, N.; Nouri, M.; Kish, M.H. Structural Characterization and Mechanical Properties of Electrospun Silk Fibroin Nanofiber Mats. *Polym. Sci. Ser. A.* **2010**, *52*, 407–412.
18. Yoshizuka, K.; Kitajou A.; Holba, M. Selective Recovery of Lithium from Seawater using a Novel MnO_2 Type Adsorbent III – Benchmark Evaluation. *Ars Separatoria Acta* **2006**, *4*, 78-85.
19. Wang, L.; Meng, C.; Ma, W. Preparation of Lithium Ion-Sieve and Utilizing in Recovery of Lithium from Seawater. *Front. Chem. Eng. China.* **2009**, *3* (1), 65-67.
20. Chitrakar, R.; Kanoh, H.; Miyai, Y.; Ooi, K. Recovery of Lithium from Seawater Using Manganese Oxide Adsorbent ($\text{H}_{1.6}\text{Mn}_{1.6}\text{O}_4$) Derived from $\text{Li}_{1.6}\text{Mn}_{1.6}\text{O}_4$. *Ind. Eng. Chem. Res.* **2001**, *40* (9), 2054-2058.
21. Chitrakar, R.; Kanoh, H.; Miyai, Y.; Ooi, K. A New Type of Manganese Oxide ($\text{MnO}_2 \cdot 0.5\text{H}_2\text{O}$) Derived from $\text{Li}_{1.6}\text{Mn}_{1.6}\text{O}_4$ and Its Lithium Ion-Sieve Properties. *Chem. Mater.* **2000**, *12*, 3151-3157.
22. Xiao, J.L.; Sun, S.Y.; Wang, J.; Li, P.; Yu, J.G. Synthesis and Adsorption Properties of $\text{Li}_{1.6}\text{Mn}_{1.6}\text{O}_4$ Spinel. *Ind. Eng. Chem. Res.* **2013**, *52*, 11967-11973.
23. Wajima, T.; Munakata, K.; Uda, T. Adsorption Behavior of Lithium from Seawater using Manganese Oxide Adsorbent. *Plasma Fusion Res.* **2012**, *7*, 2405021.
24. Lawagon, C.P.; Nisola, G.M.; Mun, J.Y.; Tron, A.; Torrejos, R.E.C.; Seo, J.G.; Kim, H.; Chung, W.-J. Adsorptive Li^+ Mining from Liquid Resources by H_2TiO_3 : Equilibrium, Kinetics, Thermodynamics, and Mechanisms. *J. Ind. Eng. Chem.* **2016**, *35*, 347-356.
25. Hong, H.J.; Park, I.S.; Ryu, T.G.; Ryu, J.H.; Kim, B.G.; Chung, K.S. Granulation of $\text{Li}_{1.33}\text{Mn}_{1.67}\text{O}_4$ (LMO) through the use of Cross-Linked Chitosan for the Effective Recovery of Li^+ from Seawater. *Chem. Eng. J.* **2013**, *234*, 16-22.

26. Umeno, A.; Miyai, Y.; Takagi, N.; Chitrakar, R.; Sakane, K.; Ooi, K. Preparation and Adsorptive Properties of Membrane-Type Adsorbents for Lithium Recovery from Seawater. *Ind. Eng. Chem. Res.* **2002**, *41*, 4281–4287.
27. Zhu, G.; Wang, P.; Qi, P.; Gao, C. Adsorption and Desorption Properties of Li⁺ on PVC-H_{1.6}Mn_{1.6}O₄ Lithium Ion-Sieve Membrane. *Chem. Eng. J.* **2014**, *235*, 340–348.
28. Park, M.J.; Nisola, G.M.; Beltran, A.B.; Torrejos, R.E.C.; Seo, J.G.; Lee, S.-P.; Kim, H.; Chung, W.-J. Recyclable Composite Nanofiber Adsorbent for Li⁺ Recovery from Seawater Desalination Retentate. *Chem. Eng. J.* **2014**, *254*, 73–81.
29. Ma, L.W.; Chen, B.Z.; Chen, Y.; Shi, X.C. Preparation, Characterization and Adsorptive Properties of Foam-Type Lithium Adsorbent. *Micropor. Mesopor. Mat.* **2011**, *142*, 147–153.
30. Han, Y.S.; Kim, H.J.; Park, J.K. Millimeter-Sized Spherical Ion-Sieve Foams with Hierarchical Pore Structure for Recovery of Lithium from Seawater. *Chem. Eng. J.* **2012**, *210*, 482–489.
31. Kim, J.H.; Oh, S.H.; Kwak, S.Y. Magnetically Separable Magnetite-Lithium Manganese Oxide Nanocomposites as Reusable Lithium Adsorbents in Aqueous Lithium Resources. *Chem. Eng. J.* **2015**, *281*, 541–548.
32. Xiao, G.; Tong, K.; Zhuo, J.; Xiao, J.; Sun, S.; Li, P.; Yu, J. Adsorption and Desorption Behavior of Lithium Ion in Spherical PVC-MnO₂ Ion Sieve. *Ind. Eng. Chem. Res.* **2012**, *51*, 10921–10929.
33. Limjuco, L.A.; Nisola, G.M.; Lawagon, C.P.; Lee, S.-P.; Seo, J.G.; Kim, H.; Chung, W.-J. H₂TiO₃ Composite Adsorbent Foam for Efficient and Continuous Recovery of Li⁺ from Liquid Resources. *Colloids Surf., A.* **2016**, *504*, 267–279.
34. Hankins, M.G.; Hayashita, T.; Kasprzyk, S.P.; Bartsch, R.A.; Immobilization of Crown Ether Carboxylic Acids on Silica Gel and Their Use in Column Concentration of Alkali Metal Cations from Dilute Aqueous Solutions. *Anal. Chem.* **1996**, *68*, 2811–2817.
35. Park, S.S.; Moorthy, M.S.; Song, H.-J.; Ha, C.-S. Functionalized Mesoporous Silicas with Crown Ether Moieties for Selective Adsorption of Lithium Ions in Artificial Sea Water. *J. Nanosci. Nanotechnol.* **2014**, *14*, 8845–8851.
36. Luo, X.; Guo, B.; Luo, J.; Deng, F.; Zhang, S.; Luo, S.; Crittenden, J. Recovery of Lithium from Wastewater Using Development of Li Ion-Imprinted Polymers, *ACS Sustainable Chem. Eng.* **2015**, *3*, 460–467.
37. Torrejos, R.E.C.; Nisola, G.M.; Park, M.J.; Shon, H.K.; Seo, J.G.; Koo, S.H.; Chung, W.-J. Synthesis and Characterization of Multi-Walled Carbon Nanotubes-Supported Dibenzo-14-Crown-4 Ether with Proton Ionizable Carboxyl Sidearm as Li⁺ Adsorbents. *Chem. Eng. J.* **2015**, *264*, 89–98.

38. Alexandratos, S.D.; Stine, C.L.; Sachleben, R.A.; Moyer, B.A.; Immobilization of Lithium-Selective 14-Crown-4 on Crosslinked Polymer Supports. *Polym.* **2005**, *46*, 6347–6352.
39. Zhou, W.; Sun, X.-L.; Gu, L.; Bao, F.-F.; Xu, X.-X.; Pang, C.-Y.; Gu, Z.-G.; Li, Z. A Green Strategy for Lithium Isotopes Separation by Using Mesoporous Silica Materials Doped with Ionic Liquids and Benzo-15-Crown-5. *J. Radioanal. Nucl. Chem.* **2014**, *300*, 843-852.
40. Pethrick, R.A.; Wilson, M.J.; Affrossman, S.; Holmes, D.; Lee, W.M. Synthesis and Cation Complexation Properties of Crown Ether Polyamic Acids/Imides. *Polym.* **2000**, *41*, 7111–7121.
41. Hayashita, T.; Goo, M.-J.; Lee, J.C.; Kim, J.S.; Krzykawski, J.; Bartsch, R.A.; Selective Sorption of Alkali-Metal Cations by Carboxylic Acid Resins Containing Acyclic or Cyclic Polyether Units. *Anal. Chem.* **1990**, *62*, 2283-2287.
42. Boda, A.; Ali, Sk.M.; Shenoi, M.R.K.; Rao, H.; Ghosh, S.K. DFT Modeling on the Suitable Crown Ether Architecture for Complexation with Cs⁺ and Sr²⁺ Metal Ions, *J. Mol. Model.* **2011**, *17*, 1091–1108.
43. Yu, H.; Whitfield, T.W.; Harder, E.; Lamoureux, G.; Vorobyov, I.; Anisimov, V.M.; MacKerell, Jr., A.D.; Roux, B. Simulating Monovalent and Divalent Ions in Aqueous Solution Using a Drude Polarizable Force Field. *J. Chem. Theory Comput.* **2010**, *6*, 774–786.